Charles University in Prague
Faculty of Mathematics and Physics

BACHELOR THESIS

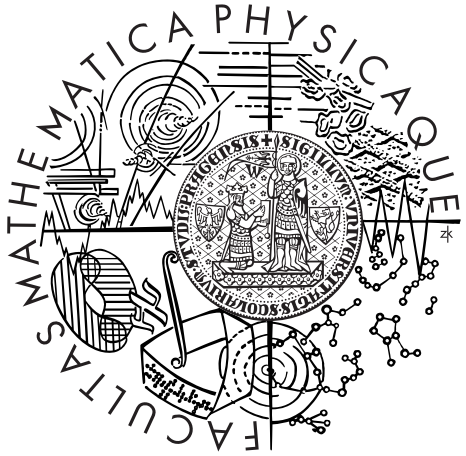

Vít Beran

Tidal heating of Neptune's moon Triton

Department of Geophysics

Supervisor of the bachelor thesis: prof. RNDr. Ondřej Čadek, CSc.
Study programme: Physics (FOF)
Specialization: Physics

Prague 2022

I thank prof. Čadek for his guidance, patience, and, above all, his willingness to supervise my thesis. I also thank my family for both moral and financial support during my studies. And last but not least, I thank my closest friends Matěj, Karel, Aleš, and Avihay for being there whenever I need them.

I declare that I carried out this bachelor thesis independently, and only with the cited sources, literature and other professional sources.

I understand that my work relates to the rights and obligations under the Act No. 121/2000 Coll., the Copyright Act, as amended, in particular the fact that the Charles University in Prague has the right to conclude a license agreement on the use of this work as a school work pursuant to Section 60 paragraph 1 of the Copyright Act.

In ..... on ..... Author signature

Název práce: Slapové zahřívání Neptunova měsíce Tritonu

Autor: Vít Beran

Katedra: Katedra geofyziky

Vedoucí bakalářské práce: prof. RNDr. Ondřej Čadek, CSc.

Abstrakt: V naší práci studujeme největší Neptunův měsíc Triton a jeho anelastickou deformaci vyvolanou pravidelným slapovým zatěžováním. Úlohu řešíme za použití spektrálních metod, vytvořili jsme náš vlastní program v jazyce Python 3 a spočítali slapové zahřívání v ledové slupce pro kondukční a konvekční přenos tepla. Zjistili jsme, že pro konduktivní modely je spočítaný výkon zanedbatelný. Nicméně pro konvekční přenos tepla jsme nalezli úzkou rodinu modelů, která predikuje spočtený 25–30 GW, což přítomnost oceánu vysvětlit nemůže, spočtený výkon však již není zanedbatlený. Dále jsme zjistili, že slapové zahřívání se koncentruje především v okolí rovníku. Vyvstává tedy otázka, zda-li to souvisí s pozorovaným kryovulkanismem a unikátním kantalupovým terénem pozorovaným na Tritonu.

Klíčová slova: slapové zahřívání, Triton, anelastická deformace, ledové měsíce

Title: Tidal heating of Neptune's moon Triton

Author: Vít Beran

Department: Department of Geophysics

Supervisor of the bachelor thesis: prof. RNDr. Ondřej Čadek, CSc.

Abstract: We study the largest Neptune's moon Triton and the anelastic deformation associated with the obliquity tides by employing spectral methods. For this purpose, we developed our Python 3 program and computed tidal heating for both conductive and convective heat transfer mechanisms in Triton's ice shell. We found that the conductive mechanism predicts marginal powers. However, we had found a family of convective models that anticipates tidal powers of 25–30 GW, which is not enough to maintain a subsurface ocean but it represents a non-negligible amount. We also found that most of the heating is concentrated around the equator, which raises the question of the connection between tidal heating and cryovolcanism and cantaloupe terrain on Triton.

Keywords: tidal dissipation, Triton, anelastic deformation, icy moons

Contents

Introduction

One of the most trending topics, not only in the academic circles, is the question of the existence of extraterrestrial life. This gave rise to a whole new scientific discipline, astrobiology, and expanded the area of focus of the planetary sciences. As it became evident that no other bodies in our vicinity are as habitable as our world, scientists started to study organisms on Earth living in extreme conditions to have a glimpse of the minimum requirements for life to occur.

In pursuit of answers, mankind has been intensively studying the Solar System for over five decades now and has launched a number of probes to both the inner and outer systems. The main objective of the probes *Voyager 1*, *Cassini*, and *Galileo* was to gather as much data as possible on Jupiter, Saturn, and their satellites, the mission *Voyager 2* closely studied the gas giant Neptune and the probe *New Horizons* was launched to expand our knowledge on Pluto, to name a few. As it was discovered that a number of the satellites in the outer system have ice-composed surfaces, these icy moons became the cynosure of the academia after it was suggested by, e.g., Lipps et al. (2004), that they might possess a reservoir of water, a subsurface ocean, that could harbor simple forms of life.

In order to keep the subsurface ocean in a liquid state, a sufficient amount of energy must be released in the body. The energy has different origins, radiogenic heating (for bodies with a large silicate core) and tidal dissipation in the ocean or the ice shell (heat generated by anelastic deformation as the body is subjected to a tidal force) are two most commonly studied processes. Jupiter's moons Ganymede, Europa, Callisto, and Saturn's moon Enceladus are the most promising candidates, and teams of scientists have consistently studied them. It has been shown that the tidal dissipation in the ice crust may generate a significant part of the heat needed to maintain the subsurface ocean in a liquid state, as discussed in, e.g., Tobie et al. (2008). However, so far very little room has been given to farther icy moons. The goal of this thesis is to study the specific case of Triton, and compute the tidal dissipation in the ice shell for various heat transfer mechanisms, compare it with the expected heat losses and estimate whether this process might possibly play an essential role in the sustainability of Triton's subsurface ocean.

Our study is divided into four chapters. The first chapter covers our contemporary knowledge of Triton. In the second chapter, we present the mathematical model; we will derive the governing equations for tidal heating from scratch and delineate the theory of anelasticity. The third chapter concerns the numerical implementation of the problem together with the validation tests. Ultimately, the fourth chapter summarizes our results for various parameters, followed by a discussion, an attached program with a brief comment, and appendices covering the advanced mathematical apparatus used in the study.

Chapter 1

Triton

Neptune was already seen and recorded by pioneers of astronomy such as Galileo Galilei (1613), Jérôme Lalande (1795), or John Herschel (1830), but initially, none of them categorized it as a planet. It was not until September 24, 1846, that the staff of the Berlin Observatory Johann Gottfried Galle and Heinrich Louis d'Arrest confirmed the existence of a major planet, Neptune, using calculations provided by the French mathematician Urbain Le Verrier. Already after seventeen days, Liverpool-based astronomer William Lassel observed and brought to the light Neptune's first satellite, later named *Triton* after the Greek god of the sea.

Until recently, we had no detailed information about the farther gas giants in the Solar System. Fortunately, that changed during the encounter of the spacecraft *Voyager 2* with Neptune in 1989. The *Voyager 2* journey played a crucial role in studying of Neptune and its satellites, for virtually all of our knowledge owed to this mission (see Stone and Miner (1989) for details). When NASA analyzed the images taken by the probe, six new satellites were found, and they claimed their places in the Neptunian family of moons, besides Triton and Nereid. The *Voyage 2* spacecraft used the radio tracking method to analyze the *total mass* (the product of the gravitational constant G and the mass) of the Neptune system and its components. It was found that Triton's average density is approximately 2.06 $\mathrm{g\,m^{-3}}$ and Triton represents essentially all of the mass orbiting Neptune. During the flyby, the probe measured the size of Triton, and with a diameter of 1353 km, Triton ranks 7th in the list of the largest icy moons in the Solar System. Triton also claims the honor of being the coldest natural body with the observed surface temperature of 38 K.

Presumably, Triton's origin lies in the Kuiper Belt and is believed to have been captured at some point since its orbit is retrograde (which is unique for the moons of greater size). Models by Vokrouhlický et al. (2008) suggest that the capture occurred 5–10 Myr after the formation of the Solar System. Immediately after the capture, the satellite had a highly eccentric orbit, which led to high tides risen upon the body by Neptune, and Triton underwent a rapid circularization process (i.e., damping of the eccentricity due to tidal dissipation). As of today, Triton ended up with a nearly perfectly circular and highly inclined orbit. The inclination of Triton is extreme, 157 °, and the satellite also has the highest obliquity (i.e., angle between the rotational axis with respect to the orbital axis) among the icy moons, e.g., Chen et al. (2014).

As the main objective of the *Voyager 2* probe was rather Neptune than Triton, and as the satellite is tidally locked, we only have information on about 40 % of the moon's surface (see Figs. 1.1 and 1.2). It appears that Triton has a tenuous atmosphere, which is presumed to be primarily composed of N_2 and CH_4 with essentially non-existing surface pressure. Triton's surface seems to be geologically young; estimates made by Schenk and Zahnle (2007) are based on the small quantity of craters, and they suggest that the age of the surface is 100 Myr at most. Triton is generally a flat body exhibiting interesting surface features (e.g. cryovolcanism) that suggest geologically interesting processes in its interior, as discussed in Cruikshank (2016). *Voyager 2* observed eruptions, located around 50°S, manifested mainly in the form of geysers of nitrogen gas in plumes, which puts Triton in a small group of bodies in our Solar System exhibiting this phenomenon.

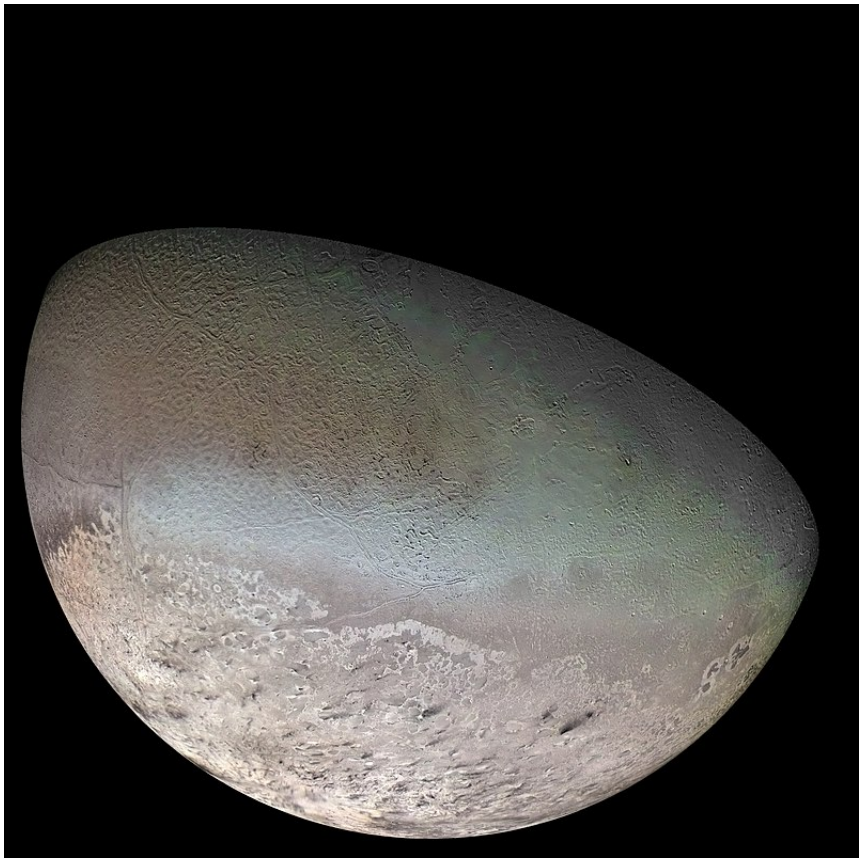

Figure 1.1: Triton reconstructed from images taken by *Voyager 2* in 1989. Adapted from Photojournal.jpl.nasa.gov (2015).

Most of Triton's observed surface on the western hemisphere is covered by a unique terrain feature (so-called *cantaloupes*) characterized by a series of long narrow depressions in the surface. This terrain comprises mostly dirty water ice, and also frozen nitrogen. Nitrogen ice is common on Triton, and the whole southern polar region is covered by it. There is a large cryovulcanic system near the equator, a caldera surrounded by a large volcan dome with the width of up to 2,000 km and two nearby cryolava lakes. This volcano, *Leviathan Patera*, is the

2nd largest in the Solar System. Additionally, the whole region is riddled with secondary volcano pits. We stress that Triton is the only body (apart from Earth) with observed cryolakes, another item on the list of Triton's unique properties. The eastern hemisphere is marked by young terrain, most likely cryolava washing over the old terrain, that is suspected to originate from Triton's interior as a result of the cryovolcanic activity. The cryolava is believed to consist of water ice and ammonia (McKinnon, 2014).

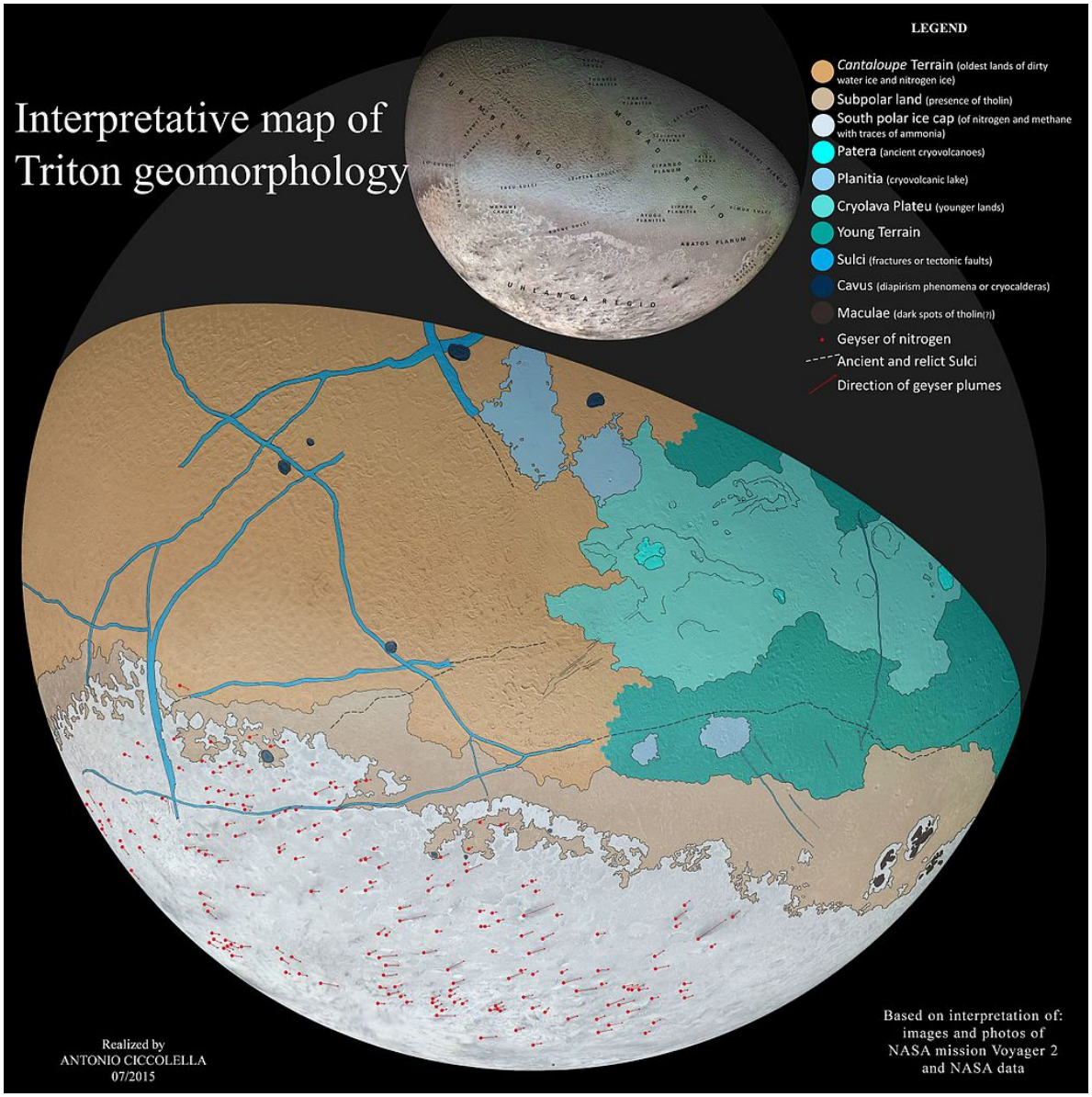

Figure 1.2: Map of the known Triton's surface (artistic impression by Antonio Cicocella, 2015). Adapted from Wikipedia (2022).

Triton is evidently an interesting body with a plethora of unique properties. To amplify our understanding of Triton and answer some of the unanswered questions, NASA's Discovery Program plans the launch of the *Trident* spacecraft on the 25th October 2025. The main objective of this mission (with a duration of 13 years) is to obtain a complete map of Triton's surface and conduct a series of measurements in the atmosphere. Also, unlike any other studied bodies, Triton gained the potential to harbor an ocean after the capture, so it might be essential to study it further. Unfortunately, the funding of this mission remains fragile and uncertain.

Chapter 2

Mathematical model and formulation

To compute the total tidal in Triton's ice shell and its contribution to the supposedly thermally stable subsurface ocean, we need to develop an appropriate physical model. The icy moon in our model is considered to be a continuous spherical body with its shell being described by the Maxwell rheological model. The shell volume is considered to be bounded within two spherical surfaces and is subject to external tidal forces. First, we will derive a set of governing equations accompanied by a pair of boundary conditions, which we will solve by employing spectral methods; we will expand the obtained equations and physical quantities in series using the formalism of spherical harmonics for unknown spectral harmonic coefficients. In the next chapter, we will use the finite difference method to express the equations on a staggered grid and virtually transform the problem into a set of algebraic equations.

2.1 Tides

In our model, we will neglect gravitational attraction with all bodies but Neptune. We can distinguish between two basic types of tides; two parameters driving the tides are eccentricity of the orbit and obliquity of the body θ_0. Since the eccentricity of Triton's orbit is effectively zero, we can only deal with the obliquity tides. The time-varying obliquity tidal potential is given by Tyler (2011) as

$$V_{\mathrm{obl}}(\vec{r},t) = -\frac{3}{2}\Omega^2 r^2 \theta_0 \sin\theta\cos\theta(\cos(\phi-\Omega t)+\cos(\phi+\Omega t)\,, \tag{2.1}$$

where Ω is the angular velocity and the potential is evaluated at a point with position vector $\vec{r} = (r,\theta,\phi)$, where r, θ, and ϕ denote the radial coordinate, co-latitude and longitude, respectively.

In the essence of section Appendix A, the potential can be rewritten, as shown in Chen et al. (2014), as

$$V_{\mathrm{obl}}(\vec{r},t) = \frac{3}{2}\sqrt{\frac{2\pi}{15}}\Omega^2 r^2 \theta_0 \left[\exp(i\Omega t)Y_{21}(\theta,\phi) - \exp(-i\Omega t)Y_{2-1}\right]\,, \tag{2.2}$$

where $Y_{2\pm1}$ denotes the scalar spherical harmonic of degree 2 and order ±1.

2.2 Governing equations

In this section, we will gradually derive the Eulerian form of the equations pertaining to the deformation of Triton's ice shell that is subject to an external periodic tidal force. This section is based on the formalism of continuity mechanics presented in Martinec (2019).

2.2.1 Reference configuration

We will consider that the body occupies the reference configuration κ_0 at time t_0 and we will assume that the stress (i.e. Cauchy stress tensor) in the body can be decomposed into two parts, prestress $\boldsymbol{\tau}_0(\vec{r}, t_0)$ and a periodically induced tidal stress $\boldsymbol{\sigma}(\vec{r}, t_0)$. If we employ the assumption that the prestress $\boldsymbol{\tau}_0$ is not time-dependent and is much greater than the incremental stress $\boldsymbol{\sigma}$, $\boldsymbol{\tau}_0$ can be used to identify the reference configuration and ought to satisfy the equilibrium relation in the shell

$$\nabla \cdot \boldsymbol{\tau}_0 + \rho_i \vec{g} = \vec{0}\,, \tag{2.3}$$

where ρ_i denotes the density of ice and $\vec{g}$ is the gravitational acceleration.

for simplicity's sake, the ice shell is considered to be regular and is bounded within two boundaries described by functions $\vec{r}_{bot}$ and $\vec{r}_{top}$ with constant radii R_{bot} and R_{top}, and the surface is considered to be stress free, thus

$$\boldsymbol{\tau}_0 \cdot \vec{e}_r = \vec{0}\,, \tag{2.4}$$

where $\vec{e}_r$ is the radial unit vector. The bottom boundary of the shell is in contact with the ocean with the density ρ_w so that the following relation must be satisfied

$$\boldsymbol{\tau}_0 \cdot \vec{e}_r = -\vec{e}_r p_0(\vec{r}_{bot})\,, \tag{2.5}$$

where $p_0(\vec{r}_{bot})$ denotes the hydrostatic pressure in the ocean acting on the bottom boundary such that

$$-\nabla p_0 + \rho_w \vec{g} = \vec{0}\,. \tag{2.6}$$

2.2.2 Present configuration

Now, we will consider that the body occupies the present configuration κ_t at time t. In this configuration, the obliquity tidal potential given by Eq. (2.1) generates an additional stress $\boldsymbol{\sigma}(\vec{r}, t)$ and displacement $\vec{u}(\vec{r}, t)$ in the ice shell. We will assume that the deformation of the body in our study is small; the Jacobian of the transformation J from κ_0 to κ_t can be linearised and expressed as

$$J \approx 1 + \nabla \cdot \vec{u}\,, \tag{2.7}$$

which allows us to write the following for the density of the deformed body

$$\rho(\vec{r}, t) = \rho_i(\vec{r})\,(1 - \nabla \cdot \vec{u})\ . \tag{2.8}$$

The equation of motion in the shell now takes the form

$$\nabla \cdot (\boldsymbol{\tau}_0 + \boldsymbol{\sigma}) + \rho\,(\vec{g} - \nabla V_{obl} - \nabla V_g) = \rho \frac{D\vec{v}}{Dt}\,, \tag{2.9}$$

where the tidal force can be expressed as the spatial gradient of the aforementioned tidal potential, V_g denotes the self-gravity potential caused by the deformation, and the right-hand side featuring velocity $\vec{v}$ is written using the material derivative operator (see Appendix C). Substituting Eqs. (2.3) and (2.8) in Eq. (2.9) yields

$$\begin{aligned} &\nabla \cdot \boldsymbol{\sigma} + \rho_i \left(-\nabla V_{obl} - \nabla V_g\right) - \rho_i \left(\nabla \cdot \vec{u}\right) \nabla (V_{obl} + V_g) - \rho_i \vec{g} \left(\nabla \cdot \vec{u}\right) = \\ &\rho_i \left(1 - \nabla \cdot \vec{u}\right) \left(\frac{\partial \vec{v}}{\partial t} + \vec{v} \cdot \nabla \vec{v}\right) . \end{aligned} \tag{2.10}$$

Provided that the velocities are small enough, we can neglect the inertial forces. Moreover, we will omit the second order term and neglect volume changes

$$\rho_i \left(\nabla \cdot \vec{u}\right) \nabla (V_{obl} + V_g) \approx \vec{0} \,, \tag{2.11}$$

$$\nabla \cdot \vec{u} \approx 0 \,. \tag{2.12}$$

The final equation of motion in the present configuration then takes the shape of

$$\nabla \cdot \boldsymbol{\sigma} - \rho_i \left(\nabla V_{obl} + \nabla V_g\right) = \vec{0} \,. \tag{2.13}$$

Additionally, the momentum equation also needs to be adjusted since the tidal potential induces periodic pressure variations in the ocean. We can write the following for the hydrostatic pressure:

$$-\nabla (p_0 + p) + \rho_w \left(\vec{g} - \nabla V_{obl} - \nabla V_g\right) = \vec{0} \,, \tag{2.14}$$

where p denotes the incremental pressure in the ocean generated by the joint action of potentials V_{obl} and V_g. By using Eq. (2.6), one obtains

$$\nabla p + \rho_w \left(\nabla V_{obl} + \nabla V_g\right) = \vec{0} \,, \tag{2.15}$$

$$p = -\rho_w \left(V_{obl} + V_g\right) \,. \tag{2.16}$$

Since the boundaries are freely deformable, the new positions of the particles in the surface and bottom layers can be expressed as $\vec{r} = \vec{r}_{bot} + \vec{u}$ and $\vec{r} = \vec{r}_{top} + \vec{u}$, respectively. On top of that, the radial unit vector alters to $\vec{e}_r + \delta\vec{e}_r$ and we can express the stress free condition in the present configuration as follows:

$$(\boldsymbol{\tau}_0 + \boldsymbol{\sigma})(\vec{r}_{top} + \vec{u}) \cdot (\vec{e}_r + \delta\vec{e}_r) = \vec{0} \,. \tag{2.17}$$

If we recall the assumption of small deformation, we can neglect the change to the radial unit vector ($\delta\vec{e}_r \approx 0$) and expand $(\boldsymbol{\tau}_0 + \boldsymbol{\sigma})(\vec{r}_{top} + \vec{u})$ in a Taylor series to first order in $\vec{u}$ about $\vec{r} = \vec{r}_{top}$, which yields

$$\begin{aligned} (\boldsymbol{\tau}_0 + \boldsymbol{\sigma})(\vec{r}_{top} + \vec{u}) \cdot \vec{e}_r &\approx \left[\boldsymbol{\tau}_0(\vec{r}_{top}) + \boldsymbol{\sigma}(\vec{r}_{top})\right] \cdot \vec{e}_r + \vec{u} \cdot \left[\nabla \boldsymbol{\tau}_0 + \nabla \boldsymbol{\sigma}\right]_{\vec{r}=\vec{r}_{top}} \cdot \vec{e}_r \\ &\approx \boldsymbol{\sigma}(\vec{r}_{top}) \cdot \vec{e}_r + \vec{u} \cdot \nabla \boldsymbol{\tau}_0|_{\vec{r}=\vec{r}_{top}} \cdot \vec{e}_r \,. \end{aligned} \tag{2.18}$$

We stress that the boundary condition is expressed at the reference surface, which allowed us to substitute Eq. (2.4) and neglect stress $\nabla \boldsymbol{\sigma}|_{\vec{r}=\vec{r}_{bot}}$, and as such requires the knowledge of the tensor $\boldsymbol{\tau}_0$. As the Cauchy stress tensor in any material can be decomposed into hydrostatic pressure p_0', viscous stress tensor $\boldsymbol{\tau}_0'$ and elastic

stress tensor (≈ 0), Eq. (2.18) can be further simplified. If we assume that $|\nabla p_0'| \approx \rho_i g \gg |\nabla \boldsymbol{\tau}_0'|$, we obtain

$$\boldsymbol{\sigma} \cdot \vec{e}_r + \rho_i \left(\vec{u} \cdot \vec{g}\right) \vec{e}_r = \boldsymbol{\sigma} \cdot \vec{e}_r + u_r \rho_i g \vec{e}_r = \vec{0} \,. \tag{2.19}$$

where we used $\vec{g} = -g\vec{e}_r$ with $\vec{e}_r = \vec{r}_{top}/|\vec{r}_{top}|$, and u_r is the radial component of the displacement vector $\vec{u}$.

The equation for the bottom boundary will be derived in an analogous manner. The condition can be expressed as

$$(\boldsymbol{\tau}_0 + \boldsymbol{\sigma})(\vec{r}_{bot} + \vec{u}) \cdot (\vec{e}_r + \delta\vec{e}_r) = -(\vec{e}_r + \delta\vec{e}_r) \left[p_0(\vec{r}_{bot} + \vec{u}) + p(\vec{r}_{bot} + \vec{u})\right] \,. \tag{2.20}$$

Neglecting the correction to the radial vector and approximating $(\boldsymbol{\tau}_0 + \boldsymbol{\sigma})(\vec{r}_{bot} + \vec{u})$ and pressures p_0, p by a first-order Taylor series in $\vec{u}$ about $\vec{r} = \vec{r}_{bot}$ leads to

$$\boldsymbol{\sigma}(\vec{r}_{bot}) \cdot \vec{e}_r + \vec{u} \cdot \nabla \boldsymbol{\tau}_0|_{\vec{r}=\vec{r}_{bot}} \cdot \vec{e}_r = -\vec{e}_r \left[p_0(\vec{r}_{bot}) + p(\vec{r}_{bot}) + \vec{u} \cdot \nabla p_0|_{\vec{r}=\vec{r}_{bot}}\right] \,. \tag{2.21}$$

By substituting Eqs. (2.6) and (2.16) in Eq. (2.21) and rearranging the terms, we obtain

$$\boldsymbol{\sigma} \cdot \vec{e}_r - u_r(\rho_w - \rho_i) g \vec{e}_r = \vec{e}_r \rho_w \left(V_{obl} + V_g\right) \,. \tag{2.22}$$

2.3 Rheology

Given the symmetry of the Cauchy stress tensor, we can define the deviatoric part $\boldsymbol{\sigma}^D$ to the tidal stress $\boldsymbol{\sigma}$ by subtracting the hydrostatic stress tensor as follows:

$$\boldsymbol{\sigma}^D = \boldsymbol{\sigma} - \left(\frac{1}{3}\sum_{i=1}^{3} \sigma_{ii}\right) \mathbf{I} \,, \tag{2.23}$$

where σ_{ii} are the diagonal components of the stress tensor $\boldsymbol{\sigma}$ and $\mathbf{I}$ denotes the identity tensor. The continuity equation and the equation of motion need to be complemented by the constitutive equation, which describes the typical behavior of the material in the model. We will deal with the elastic model (Hooke's law, used later in the validation tests) and the Maxwell viscoelastic model, which is traditionally used in the planetology sciences in the studies of ice shells anelastic deformation. The elastic model is described by

$$\boldsymbol{\sigma}^D - \mu \left(\nabla \vec{u} + (\nabla \vec{u})^T\right) = 0 \,, \tag{2.24}$$

where μ is the shear modulus and the gradient of a vector is understood as a second-order tensor. The left-hand side of the Maxwell viscoelastic model is formally identical to the elastic model, however, there is an additional memory term

$$\boldsymbol{\sigma}^D - \mu \left(\nabla \vec{u} + (\nabla \vec{u})^T\right) = -\frac{\mu}{\eta} \int_0^t \boldsymbol{\sigma}^D(t') \, \mathrm{d}t' \,. \tag{2.25}$$

2.4 Viscosity and temperature

In our study, we will consider two temperature profiles reflecting the examined heat transfer mechanisms. The shell is considered to be in a thermal quasi-equilibrium ($\partial T/\partial t \approx 0$) in both cases. The conductive profile is obtained as the

analytic solution of the heat equation in spherical coordinates with temperature non-dependent conductivity k, $\nabla^2 T \approx 0$, given by

$$T(r) = \frac{A}{r} + B, \qquad T(r) \approx Ar + B\,, \tag{2.26}$$

where the latter holds for the region of low thickness. The constants A and B are determined from the boundary conditions, temperatures on the surface and the bottom boundary $T(R_{top}) = T_{top}$ and $T(R_{bot}) = T_{bot}$.

The convective profile is a lot more complicated, the heat equation now reads $0 \approx \vec{v} \cdot \nabla T$. Given the dot product in the convective term, the profile is characterized by two conductive layers (1/3 and 1/10 of the shell thickness h in our model) of linear decrease in the temperature. The temperature remains nearly unchanged in the rest of the shell (for simplicity, we neglect the changes completely). The scheme of the approximate profile is in Fig. 2.1.

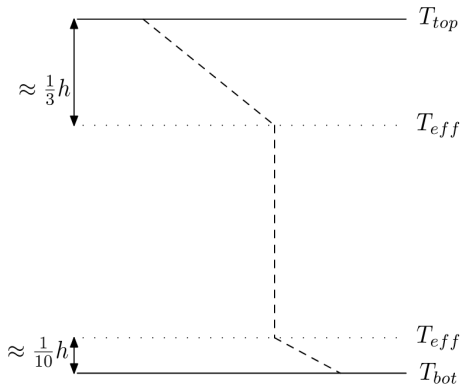

Figure 2.1: Convective temperature profile for a shell of thickness h and temperature T_{eff}, at which the conduction process stops. The reader should be aware that the sketch is solely illustrative, for the temperature derivative needs to be defined everywhere (i.e., the heat flux is continuous).

The knowledge of the temperature model is crucial for determining the viscosity profile in the shell. Viscosity is considered to depend only on temperature, and solely the diffusion creep is taken into account. To describe this, we will utilize the Arrhenius law in the following form taken from Souček et al. (2019):

$$\eta(T) = \eta_0 \exp\left[\frac{E}{RT_{bot}}\left(\frac{T_{bot}}{T} - 1\right)\right], \tag{2.27}$$

where R is the gas constant, $E = 59$ kJ/mol^{-1} is the activation energy for the diffusion creep (see Goldsby and Kohlstedt (2001) for details), and $\eta_0 \in (10^{13} - 10^{17})$ Pa is the basal viscosity at temperature T_{bot}. Since the values of viscosity skyrocket for low temperatures, a viscosity cutoff of $\eta_{cut} = 10^{20}$ Pa has to be imposed so that $\eta \leq \eta_{cut}$ always holds.

2.5 Tidal dissipation

The average tidal dissipation at a point $\vec{r}$ is given by (e.g., Souček et al., 2019)

$$H_t(\vec{r}) = \frac{1}{P}\int_{t_1}^{t_1+P} \frac{\boldsymbol{\sigma}^D(\vec{r},t) : \boldsymbol{\sigma}^D(\vec{r},t)}{2\eta(\vec{r})}\,\mathrm{d}t\,, \tag{2.28}$$

where P is Triton's orbital period and $t_1 \gg P$ denotes an arbitrary time once the system reaches a periodically stable state, and the double dot product is understood as the contraction of tensors $\boldsymbol{\sigma}^D$ with respect to the first/last two indices of the second/first tensor. Thus

$$\boldsymbol{\sigma}^D : \boldsymbol{\sigma}^D = \sum_{i=1}^{3}\sum_{j=1}^{3} \sigma_{ij}^D \sigma_{ji}^D \,, \tag{2.29}$$

where σ_{ij}^D are the components of the deviatoric tensor. The total average dissipation is obtained by integrating over the volume V of the shell

$$H_{tot} = \frac{1}{P}\int_{t_1}^{t_1+P}\int_V \frac{\boldsymbol{\sigma}^D(\vec{r},t) : \boldsymbol{\sigma}^D(\vec{r},t)}{2\eta(\vec{r})}\,\mathrm{d}V\,\mathrm{d}t\,. \tag{2.30}$$

Furthermore, we can formally determine the tidal heat flux as

$$q_t(\theta,\phi) = \frac{1}{R_{top}^2}\int_{R_{bot}}^{R_{top}} H_t(\vec{r}) r^2\,\mathrm{d}r\,. \tag{2.31}$$

2.6 Spectral analysis

Now, Eqs. (2.12), (2.13), (2.19), (2.22), (2.25) represent a complete PDE system of our model. In the spirit of section Appendix A, we will expand the physical quantities in harmonic series

$$\vec{f}(r,\theta,\phi) = \sum_{j=0}^{\infty}\sum_{m=-j}^{j}\sum_{l=|j-1|}^{j+1} f_{jm}^l(r)\vec{Y}_{jm}^l(\theta,\phi)\,, \tag{2.32}$$

$$\vec{u}(r,\theta,\phi) = \sum_{j=0}^{\infty}\sum_{m=-j}^{j}\sum_{l=|j-1|}^{j+1} u_{jm}^l(r)\vec{Y}_{jm}^l(\theta,\phi)\,, \tag{2.33}$$

$$\boldsymbol{\sigma}(r,\theta,\phi) = \sum_{j=0}^{\infty}\sum_{m=-j}^{j}\sum_{k=0,2}\sum_{l=|j-k|}^{j+k} t_{jm}^{lk}(r)\mathbf{Y}_{jm}^{lk}(\theta,\phi)\,, \tag{2.34}$$

$$\boldsymbol{\sigma}^D(r,\theta,\phi) = \sum_{j=0}^{\infty}\sum_{m=-j}^{j}\sum_{l=|j-2|}^{j+2} t_{jm}^{l2}(r)\mathbf{Y}_{jm}^{l2}(\theta,\phi)\,. \tag{2.35}$$

By substituting Eqs. (2.32)–(2.35) in Eqs. (2.12), (2.13), (2.19), (2.22), (2.25), we obtain a set of spectrally decomposed equations. Within the framework of spectral analysis, we have to deal with the acting of various differential operators on scalar, vector, and tensor spherical harmonics. The exact formulae used whilst processing the governing equations are listed in Appendix C. Similarly, we will expand the gravitational potential due to the deformation of the top and bottom boundaries as follows (e.g., Čadek et al., 2021):

$$\begin{aligned} V^{(top)}(r,\theta,\phi) &= \sum_{j=0}^{\infty}\sum_{m=-j}^{j} V_{jm}^{(top)}(r) Y_{jm}(\theta,\phi) \\ &= \sum_{j=0}^{\infty}\sum_{m=-j}^{j}\left[-\frac{4\pi G\rho_i r}{2j+1}\left(\frac{r}{R_{top}}\right)^{j-1}(u_r)_{jm}^{(top)}\right] Y_{jm}(\theta,\phi)\,, \end{aligned} \tag{2.36}$$

$$V^{(bot)}(r,\theta,\phi) = \sum_{j=0}^{\infty}\sum_{m=-j}^{j} V_{jm}^{(bot)}(r) Y_{jm}(\theta,\phi)$$
$$= \sum_{j=0}^{\infty}\sum_{m=-j}^{j}\left[-\frac{4\pi G(\rho_w-\rho_i)r}{2j+1}\left(\frac{R_{bot}}{r}\right)^{j+1}(u_r)_{jm}^{(bot)}\right] Y_{jm}(\theta,\phi)\,, \tag{2.37}$$

where G is the gravitational constant and the spectral form of the radial component of the displacement vector is given by

$$u_r = \vec{e}_r\cdot\vec{u} = \sum_{jm}\left(\sqrt{\frac{j}{2j+1}}u_{jm}^{j-1} - \sqrt{\frac{j+1}{2j+1}}u_{jm}^{j+1}\right) Y_{jm}\,. \tag{2.38}$$

Looking at Eq. (2.2) insinuates that the deformation only arises for $j=2$. In spite of that, we will carry on writing everything in a general manner. The tidal deformation is assumed to be axially symmetric, therefore, we can neglect the toroidal equations (i.e., neglecting equations for $v_{jm}^{j}, t_{jm}^{j-1,2}$. and $t_{jm}^{j+1,2}$) and solve only a system of spheroidal equations (i.e., equations for v_{jm}^{j-1}, v_{jm}^{j+1}, t_{jm}^{j0}, $t_{jm}^{j-2,2}$, t_{jm}^{j2}, and $t_{jm}^{j+2,2}$). All equations are now expressed for each degree j and order m separately:

$$\sqrt{\frac{j}{2j+1}}\left(\frac{\mathrm{d}}{\mathrm{d}r}-\frac{j-1}{r}\right)u_{jm}^{j-1} - \sqrt{\frac{j+1}{2j+1}}\left(\frac{\mathrm{d}}{\mathrm{d}r}+\frac{j+2}{r}\right)u_{jm}^{j+1} = 0\,, \tag{2.39}$$

$$\begin{aligned}&-\sqrt{\frac{j}{3(2j+1)}}\left(\frac{\mathrm{d}}{\mathrm{d}r}+\frac{j+1}{r}\right)t_{jm}^{j0} + \sqrt{\frac{j-1}{2j-1}}\left(\frac{\mathrm{d}}{\mathrm{d}r}-\frac{j-2}{r}\right)t_{jm}^{j-2,2}\\ &-\sqrt{\frac{(j+1)(2j+3)}{6(2j-1)(2j+1)}}\left(\frac{\mathrm{d}}{\mathrm{d}r}+\frac{j+1}{r}\right)t_{jm}^{j2} + f_{jm}^{j-1}(t) = 0\,,\end{aligned} \tag{2.40}$$

$$\begin{aligned}&\sqrt{\frac{j+1}{3(2j+1)}}\left(\frac{\mathrm{d}}{\mathrm{d}r}-\frac{j}{r}\right)t_{jm}^{j0} + \sqrt{\frac{j(2j-1)}{6(2j+1)(2j+3)}}\left(\frac{\mathrm{d}}{\mathrm{d}r}-\frac{j}{r}\right)t_{jm}^{j2}\\ &-\sqrt{\frac{j+2}{2j+3}}\left(\frac{\mathrm{d}}{\mathrm{d}r}+\frac{j+3}{r}\right)t_{jm}^{j+2,2} + f_{jm}^{j+1}(t) = 0\,.\end{aligned} \tag{2.41}$$

$$t_{jm}^{j-2,2} - 2\mu\sqrt{\frac{j-1}{2j-1}}\left(\frac{\mathrm{d}}{\mathrm{d}r}+\frac{j}{r}\right)u_{jm}^{j-1} = -\frac{\mu}{\eta}\int_0^t t_{jm}^{j-2,2}(t',r)\,\mathrm{d}t'\,, \tag{2.42}$$

$$\begin{aligned}&t_{jm}^{j2} + 2\mu\sqrt{\frac{(j+1)(2j+3)}{2.3.(2j-1)(2j+1)}}\left(\frac{\mathrm{d}}{\mathrm{d}r}-\frac{j-1}{r}\right)u_{jm}^{j-1}\\ &-2\mu\sqrt{\frac{j(2j-1)}{2.3.(2j+1)(2j+3)}}\left(\frac{\mathrm{d}}{\mathrm{d}r}+\frac{j+2}{r}\right)u_{jm}^{j+1} = -\frac{\mu}{\eta}\int_0^t t_{jm}^{j2}(t',r)\,\mathrm{d}t'\,,\end{aligned} \tag{2.43}$$

$$t_{jm}^{j+2,2} + 2\mu\sqrt{\frac{j+2}{2j+3}}\left(\frac{\mathrm{d}}{\mathrm{d}r} - \frac{j+1}{r}\right) u_{jm}^{j+1} = -\frac{\mu}{\eta}\int_0^t t_{jm}^{j+2,2}(t', r)\ \mathrm{d}t' \,. \tag{2.44}$$

$$\begin{aligned} &-\sqrt{\frac{j}{3(2j+1)}}t_{jm}^{j0} - \sqrt{\frac{(j+1)(2j+3)}{6(2j+1)(2j-1)}}t_{jm}^{j2} + \sqrt{\frac{j-1}{2j-1}}t_{jm}^{j-2,2} \\ &+ \frac{\rho_i g_s}{2j+1} j u_{jm}^{j-1} - \frac{\rho_i g_s}{2j+1}\sqrt{j(j+1)}u_{jm}^{j+1} = 0 \,, \end{aligned} \tag{2.45}$$

$$\begin{aligned} &\sqrt{\frac{j+1}{3(2j+1)}}t_{jm}^{j0} + \sqrt{\frac{j(2j-1)}{6(2j+1)(2j+3)}}t_{jm}^{j2} - \sqrt{\frac{j+2}{2j-1}}t_{jm}^{j+2,2} \\ &+ \frac{\rho_i g_s}{2j+1}\sqrt{j(j+1)}u_{jm}^{j-1} - \frac{\rho_i g_s}{2j+1}(j+1)u_{jm}^{j+1} = 0 \,, \end{aligned} \tag{2.46}$$

$$\begin{aligned} &\sqrt{\frac{j}{3(2j+1)}}t_{jm}^{j0} + \sqrt{\frac{(j+1)(2j+3)}{6(2j+1)(2j-1)}}t_{jm}^{j2} - \sqrt{\frac{j-1}{2j-1}}t_{jm}^{j-2,2} \\ &+ \frac{(\rho_w - \rho_i)g_b}{2j+1} j u_{jm}^{j-1} - \frac{(\rho_w - \rho_i)g_b}{2j+1}\sqrt{j(j+1)}u_{jm}^{j+1} \\ &= \sqrt{\frac{j}{2j+1}}\rho_w \left[V_{obl}(t, R_{bot}) + V^{(top)}(R_{bot}) + V^{(bot)}(R_{bot})\right] \,, \end{aligned} \tag{2.47}$$

$$\begin{aligned} &-\sqrt{\frac{j+1}{3(2j+1)}}t_{jm}^{j0} - \sqrt{\frac{j(2j-1)}{6(2j+1)(2j+3)}}t_{jm}^{j2} + \sqrt{\frac{j+2}{2j-1}}t_{jm}^{j+2,2} \\ &- \frac{(\rho_w - \rho_i)g_b}{2j+1}\sqrt{j(j+1)}u_{jm}^{j-1} + \frac{(\rho_w - \rho_i)g_b}{2j+1}(j+1)u_{jm}^{j+1} \\ &= -\sqrt{\frac{j+1}{2j+1}}\rho_w \left[V_{obl}(t, R_{bot}) + V^{(top)}(R_{bot}) + V^{(bot)}(R_{bot})\right] \,, \end{aligned} \tag{2.48}$$

where Eq. (2.39) is the continuity equation, Eqs. (2.40) and (2.41) are the equations of motion, Eqs. (2.42)–(2.44) rheology equations, and at last Eqs. (2.45)–(2.48) are the decomposed boundary conditions. Since we are going to conduct a parametric study (i.e., including models with great shell thickness), we distinguish between gravitational acceleration on the surface g_s and at the bottom boundary g_b, which is estimated by

$$g_b(R_{bot}) \approx \frac{4}{3} G \rho_{avg} R_{bot} \,, \tag{2.49}$$

where ρ_{avg} is Triton's average density.

The body forces in our system stem from the tidal and self-gravity potential and, as such, can be expressed as the spatial gradients $\vec{f} = -\rho_i \nabla V$ (for details,

see Appendix C). The spectral form of the obliquity tidal force is acquired using Eq. (2.1) as

$$f^1_{21} = \sqrt{3\pi}\rho_i r\Omega^2\theta_0 \left(\cos(\Omega t) + i\sin\Omega t\right)\vec{Y}^1_{21}\,. \tag{2.50}$$

Similarly, we will calculate the spectral form of the body forces due to the deformation of the surface and bottom boundary using Eqs. (2.36) and (2.37), respectively,

$$f^{j-1}_{jm} = 4\pi\rho_i^2 G u_r^{(top)} \sqrt{\frac{j}{2j+1}} \left(\frac{r}{R_{top}}\right)^{j-1} \vec{Y}^{j-1}_{jm}\,, \tag{2.51}$$

$$f^{j+1}_{jm} = 4\pi\rho_i(\rho_w - \rho_i) G u_r^{(bot)} \sqrt{\frac{j+1}{2j+1}} \left(\frac{R_{bot}}{r}\right)^{j+2} \vec{Y}^{j+1}_{jm}\,, \tag{2.52}$$

where we substitute $j = 2$ and $m = 1$. Analogously, we will use the global condition of orthonormality of tensor harmonics to derive the spectral form of the formula for the total tidal heating, which yields

$$H_{tot} = \frac{1}{P}\sum_{jml}\int_{t_1}^{t_1+P}\int_{R_{bot}}^{R_{top}} \frac{t^{l2}_{jm}(r,t)\,t^{l2*}_{jm}(r,t)}{2\eta(r)} r^2\,\mathrm{d}r\,\mathrm{d}t\,. \tag{2.53}$$

We will want to compare the computed power with the energy losses due to body radiation, which can be estimated by calculating the heat flux $\vec{q} = -k\nabla T$ at the surface and integrating over the entire sphere S, thus

$$\mathcal{P} = \int_S \vec{q}\cdot\mathrm{d}\vec{S} = 4\pi R^2_{top} k \frac{\mathrm{d}T}{\mathrm{d}r}\,. \tag{2.54}$$

To assess the compatibility of our computed models, we will use the Rayleigh number defined by

$$\mathrm{Ra} = \frac{\rho_i \alpha g (T_{bot} - T_{top}) d^3}{\kappa\eta_0}\,, \tag{2.55}$$

where α is the thermal expansivity of ice and κ denotes the thermal diffusivity. Parameters thickness d and viscosity η_0 at the base of the shell determine the Rayleigh number, which can be perceived as the probability of the occurrence of the convective mechanism; once the Rayleigh number drops below some critical value Ra_{cr}, the convective processes cease.

Chapter 3

Numerical implementation

This chapter is devoted to the numerical implementation of our model. The section covers the detailed description of the used numerical methods, technical details, and also the validation tests used to demonstrate the correctness of our program (see Attachment).

3.1 Numerical model

The uniformly discretized ice shell comprises N interfaces, separated by distance Δr, and $N-1$ layers is depicted in Fig. 3.1. The vector quantities (i.e., body force $\vec{f}$ and displacement $\vec{u}$) are being evaluated in the centers of layers, whereas the scalar and tensor variables (i.e., stress coefficients $t^{j0}_{jm}, t^{j2}_{jm}, t^{j\pm2,2}_{jm}$ and material properties η, μ) on the interfaces. For brevity, we will employ the following notation:

$$v^{j\pm1}_{jm}(r_i) = v^{\pm}_i \;\; f^{j\pm1}_{jm}(r_i) = f^{\pm}_i \;\; t^{j\pm2,2}_{jm}(r_i) = t^{\pm2}_i \;\; t^{j2}_{jm}(r_i) = t^{2}_i \;\; t^{j0}_{jm}(r_i) = t^{0}_i \,. \quad (3.1)$$

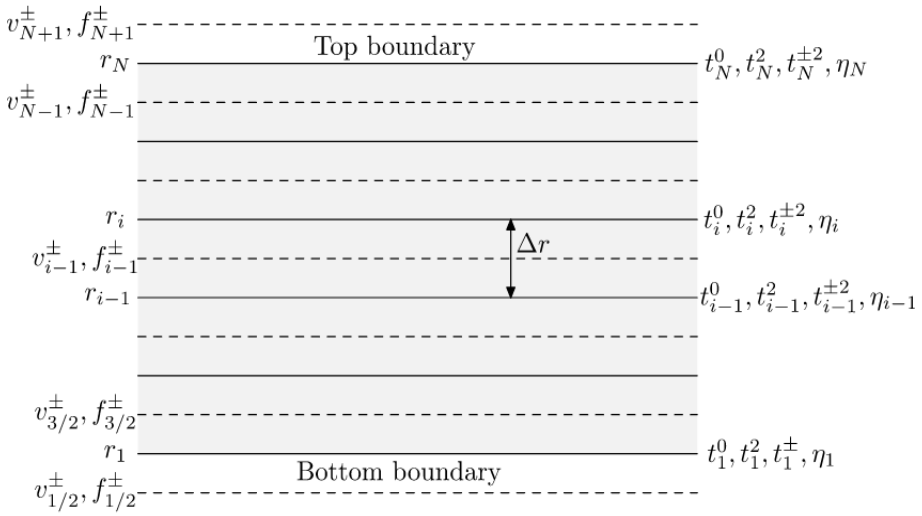

Figure 3.1: Radial discretization of the ice shell (delineated by shallow white) - N interfaces (solid lines), $N-1$ layers (dashed lines) and two fictitious lines (i.e., staggered grid of the first order)

The indexing goes in the ascending order and follows the logic of the decomposed equations (i.e., bottom boundary divides the shell from the ocean). Furthermore, we will apply the finite difference method to approximate the derivatives and functional values by the neighboring values on the grid. Let us suppose that f and g are functions we want to approximate on the $i-$th interface and in the middle of the $i-$th layer, respectively, where $i = 1, 2, \ldots, N$. The radial derivatives and the functional values can then be expressed as

$$\left.\frac{\partial f}{\partial r}\right|_{r=r_i} \approx \frac{f_i - f_{i+1}}{\Delta r}\,, \quad f(r_i) \approx \frac{f_i + f_{i+1}}{2}\,, \tag{3.2}$$

$$\left.\frac{\partial g}{\partial r}\right|_{r=r_i+\Delta r/2} \approx \frac{g_{i-1} - g_i}{\Delta r}\,, \quad g(r_i + \Delta r/2) \approx \frac{g_{i+1} - g_i}{2}\,. \tag{3.3}$$

The Maxwell rheology we are using in our study is characterized by the memory term given by a time integral. In order to numerically evaluate this integral, we will utilize the trapezoidal rule. If we discretize the time domain t into n intervals (each of length Δt), the integral can be approximated by

$$\frac{\mu}{\eta}\int_0^t \boldsymbol{\sigma}^D(t')\ \mathrm{d}t' \approx \frac{\mu}{\eta}\Delta t \sum_{i=1}^{n-1}\left(\boldsymbol{\sigma}^D_{i-1} + \boldsymbol{\sigma}^D_i\right)\,. \tag{3.4}$$

Similarly, the integral in the formula Eq. (2.30) for total dissipation is roughly equal to

$$\int_{R_{bot}}^{R_{top}} \lambda(r) r^2\ \mathrm{d}r \approx \lambda(R_{bot}) R_{bot}^2 \frac{\Delta r}{2} + \sum_{i=2}^{N-1} \lambda(r_i) r_i^2 \Delta r + \lambda(R_{top}) R_{top}^2 \frac{\Delta r}{2}\,, \tag{3.5}$$

where $\lambda(r)$ denotes the whole integrand.

Subsequently, we will process all spectral equations Eqs. (2.39)–(2.48) and obtain N continuity equations, $3N$ rheology equations, $2(N-1)$ equations of motion, and 4 boundary conditions, thus, $6N+2$ equations in total, which coincides with the number of variables (i.e., the algebraic system is complete). These equations can be organized in a band matrix Fig. 3.2, which we will solve efficiently using the SciPy module `solve_banded` and the low-level Fortran subroutine `zgbsv` (`http://www.netlib.org/lapack`). Moreover, we slightly alter the notation for stress coefficients in the rheology equations by adding a second index referring to the time domain discretization. For the sake of brevity, we will employ a coefficient nomenclature (see Appendix D), thus

$$\begin{aligned}&\left(\frac{a_2}{2r_i} - \frac{a_1}{\Delta r}\right) u^-_{i-1/2} \\ &\quad + \left(\frac{b_2}{2r_i} - \frac{b_1}{\Delta r}\right) u^+_{i-1/2} + \left(\frac{a_2}{2r_i} + \frac{a_1}{\Delta r}\right) u^-_{i+1/2} + \left(\frac{b_2}{2r_i} + \frac{b_1}{\Delta r}\right) u^+_{i+1/2} = 0\,,\end{aligned} \tag{3.6}$$

$$\begin{aligned}-\frac{1}{\eta_i}\left(\frac{1}{2}t^{-2}_{i,0}\Delta t + \sum_{j=1}^{n-1} t^{-2}_{i,j}\Delta t\right) &= \left(\frac{1}{\mu} + \frac{\Delta t}{4\eta_i}\right) t^{-2}_{i,n} + \\ &\quad + \left(\frac{p_2}{2r_i} - \frac{p_1}{\Delta r}\right) u^-_{i-1/2} + \left(\frac{s_2}{2r_i} - \frac{s_1}{\Delta r}\right) u^+_{i-1/2}\,,\end{aligned} \tag{3.7}$$

$$-\frac{1}{\eta_i}\left(\frac{1}{2}t^{+2}_{i,0}\Delta t+\sum_{j=1}^{n-1}t^{+2}_{i,j}\Delta t\right)=\left(\frac{1}{\mu}+\frac{\Delta t}{4\eta_i}\right)t^{+2}_{i,n}+ \\ +\left(\frac{p_2}{2r_i}-\frac{p_1}{\Delta r}\right)u^{-}_{i-1/2}+\left(\frac{s_2}{2r_i}-\frac{s_1}{\Delta r}\right)u^{+}_{i-1/2}\,, \tag{3.8}$$

$$-\frac{1}{\eta_i}\left(\frac{1}{2}t^{2}_{i,0}\Delta t+\sum_{j=1}^{n-1}t^{2}_{i,j}\Delta t\right)=\left(\frac{1}{\mu}+\frac{\Delta t}{4\eta_i}\right)t^{2}_{i,n}+ \\ +\left(\frac{q_2}{2r_i}-\frac{q_1}{\Delta r}\right)u^{-}_{i-1/2}+\left(\frac{r_2}{2r_i}-\frac{r_1}{\Delta r}\right)u^{+}_{i-1/2} \\ +\left(\frac{q_2}{2r_i}+\frac{q_1}{\Delta r}\right)u^{-}_{i+1/2}+\left(\frac{r_2}{2r_i}+\frac{r_1}{\Delta r}\right)u^{+}_{i+1/2}\,, \tag{3.9}$$

$$\left(\frac{c_2}{2r_{i+1/2}}-\frac{c_1}{\Delta_r}\right)t^{0}_{i,n}+ \\ +\left(\frac{d_2}{2r_{i+1/2}}-\frac{d_1}{\Delta r}\right)t^{-2}_{i,n}+\left(\frac{e_2}{2r_{i+1/2}}-\frac{e_1}{\Delta r}\right)t^{2}_{i,n}+\left(\frac{c_2}{2r_{i+1/2}}+\frac{c_1}{\Delta_r}\right)t^{0}_{i+1,n} \\ +\left(\frac{d_2}{2r_{i+1/2}}+\frac{d_1}{\Delta r}\right)t^{-2}_{i+1,n}+\left(\frac{e_2}{2r_{i+1/2}}+\frac{e_1}{\Delta r}\right)t^{2}_{i+1,n}=-f^{-}_{i+1/2}\,, \tag{3.10}$$

$$\left(\frac{f_2}{2r_{i+1/2}}-\frac{f_1}{\Delta_r}\right)t^{0}_{i,n}+ \\ +\left(\frac{g_2}{2r_{i+1/2}}-\frac{g_1}{\Delta r}\right)t^{2}_{i,n}+\left(\frac{h_2}{2r_{i+1/2}}-\frac{h_1}{\Delta r}\right)t^{+2}_{i,n}+\left(\frac{f_2}{2r_{i+1/2}}+\frac{f_1}{\Delta_r}\right)t^{0}_{i+1,n} \\ +\left(\frac{g_2}{2r_{i+1/2}}+\frac{g_1}{\Delta r}\right)t^{2}_{i+1,n}+\left(\frac{h_2}{2r_{i+1/2}}+\frac{h_1}{\Delta r}\right)t^{+2}_{i+1,n}=-f^{+}_{i+1/2}\,. \tag{3.11}$$

$$\frac{1}{2}z_1\left(u^{-}_{n+1/2}+u^{-}_{n-1/2}\right)+\frac{1}{2}z_2\left(u^{+}_{n+1/2}+u^{+}_{n-1/2}\right)+z_3t^{0}_{1}+z_4t^{-2}_{1}+z_5t^{2}_{1}=0\,, \tag{3.12}$$

$$\frac{1}{2}w_1\left(u^{-}_{n+1/2}+u^{-}_{n-1/2}\right)+\frac{1}{2}w_2\left(u^{+}_{n+1/2}+u^{+}_{n-1/2}\right)+w_3t^{0}_{1,n}+w_4t^{2}_{1,n}+w_5t^{+2}_{1,n}=0\,, \tag{3.13}$$

$$\frac{1}{2}x_1\left(u^{-}_{3/2}+u^{-}_{1/2}\right)+\frac{1}{2}x_2\left(u^{+}_{3/2}+u^{+}_{1/2}\right)+ \\ +x_3t^{0}_{1,n}+x_4t^{-2}_{1,n}+x_5t^{2}_{1,n}=\delta_1\left[V_{obl}(t,R_{bot})+V^{(top)}(R_{bot})+V^{(bot)}(R_{bot})\right]\,, \tag{3.14}$$

$$\frac{1}{2}y_1\left(u^{-}_{3/2}+u^{-}_{1/2}\right)+\frac{1}{2}y_2\left(u^{+}_{n+1/2}+u^{+}_{n-1/2}\right)+ \\ +y_3t^{0}_{1,n}+y_4t^{2}_{1,n}+y_5t^{+2}_{1,n}=\delta_2\left[V_{obl}(t,R_{bot})+V^{(top)}(R_{bot})+V^{(bot)}(R_{bot})\right]\,, \tag{3.15}$$

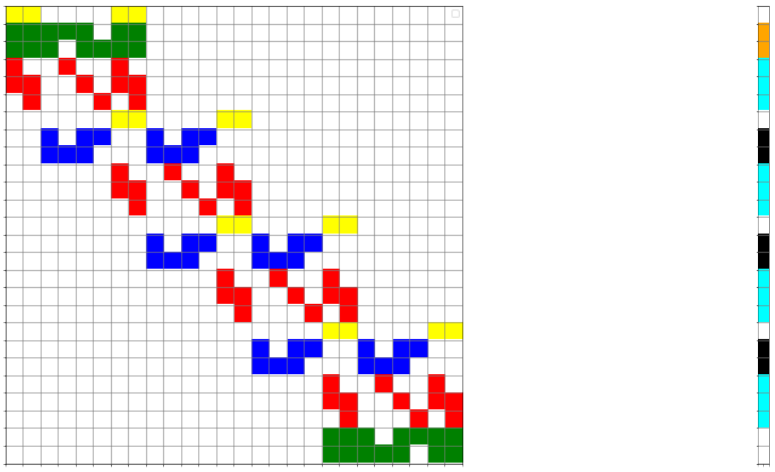

(a) Band matrix $(6N+2)^2$ (b) Right-hand side $(6N+2)$

Figure 3.2: (a) The structure of the band matrix ($N = 4$): the coefficients organized in columns correspond to $u_i^-, u_i^+, t_i^0, t_i^\pm, t_i^2$. Green (boundary conditions), yellow (continuity equations), red (rheology equations), and blue (equations of motion) (b) The right-hand side ($N = 4$): orange (bottom boundary conditions: time-dependent tidal potential V_{obl} and self-gravity potential V_g updated in each time step), cyan (integration in the rheology equations), and black (equations of motion: f_{21}^1 accounts for the tidal force and internal gravitational potential, f_{21}^3 originates from the external gravitational potential).

where Eq. (3.6) is the continuity equation, Eqs. (3.7)–(3.9) rheology equations, Eqs. (3.10) and (3.11) are the equations of motion, and Eqs. (3.12)–(3.15) are the boundary conditions. The band matrix T of the system has the following structure:

$$\mathrm{T} = \begin{pmatrix} \text{continuity equation} \\ 2 \times \text{bottom boundary condition} \\ (N-1) \times \begin{cases} \text{continuity equation} \\ \text{3x rheology equations} \\ \text{equations of motion} \end{cases} \\ \text{continuity equation} \\ \text{3x rheology equations} \\ 2 \times \text{top boundary condition} \end{pmatrix} \tag{3.16}$$

Finally, the radial displacement u_r featured in the equations describing the self-gravity effect is always estimated from the last time step. At the end of each cycle, we calculate the radial displacement u_r using Eq. (2.38) and update the potential V_g in the bottom boundary condition.

3.2 Validation test

Our program was tested against several benchmarks provided by prof. Ondřej Čadek that he computed using a similar program of his. For illustration purposes, we selected the following benchmark - elastic deformation due to the periodic obliquity tidal force f_{21}^1 given by Eq. (2.50). The parameters of the model are listed below in Tab. 3.1.

Table 3.1: Parameters used for the validation test

Parameter	Notation	Value	Unit
Density of water	ρ_w	998	$\mathrm{kg\,m^{-3}}$
Density of ice	ρ_i	916.8	$\mathrm{kg\,m^{-3}}$
Gravitational acceleration	g	0.78	$\mathrm{m\,s^{-2}}$
Orbital period	P	5.875	days
Obliquity	θ_0	0.35	°
Shear modulus	μ	$3.3 \cdot 10^9$	Pa
Inner radius	R_{bot}	900	km
Outer radius	R_{top}	1300	km

We had the program run for the duration of one orbital period and computed the radial displacement for each interface. The match of the solutions is demonstrated for the real part of the surface and bottom topography in Fig. 3.3.

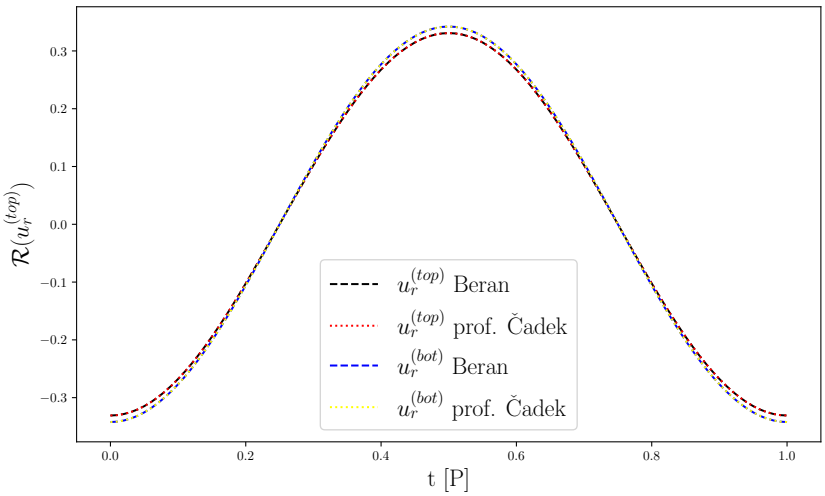

Figure 3.3: Elastic benchmark

Chapter 4

Results

In this section, we will investigate the model of Triton's ice shell with a subsurface ocean. The list of parameters and their values used in this study are listed below in Tab. 4.1.

Table 4.1: Parameters used in the study

Parameter	Notation	Value	Unit
Density of water[1]	ρ_w	1000	$\mathrm{kg\,m^{-3}}$
Density of ice[1]	ρ_i	920	$\mathrm{kg\,m^{-3}}$
Triton's average density[2]	ρ_i	2060	$\mathrm{kg\,m^{-3}}$
Grav. acceleration (at the top)[2]	g_s	0.78	$\mathrm{m\,s^{-2}}$
Grav. acceleration (at the bottom)	g_b	See Eq. (2.49)	$\mathrm{m\,s^{-2}}$
Orbital period[2]	P	5.875	days
Obliquity[2]	θ_0	-0.35	$^\circ$
Shear modulus[3]	μ	$3.3 \cdot 10^9$	Pa
Inner radius	R_{bot}	900 – 1345	km
Outer radius[2]	R_{top}	1350	km
Thermal conductivity[4]	k	2.2	$\mathrm{W\,m^{-1}\,K^{-1}}$
Basal viscosity	η	See Eq. (2.27)	Pa s
Surface temperature[5]	T_{top}	38	K
Melting temperature of ice[6]	T_{bot}	273	K
Temperature (convective mode)[7]	T_{eff}	250	K
Number of layers	N	100	–
Thermal diffusivity of ice[8]	κ	$1.1 \cdot 10^{-6}$	$\mathrm{m^2\,s^{-1}}$
Thermal expansivity of ice[8]	α	$1.6 \cdot 10^{-4}$	$\mathrm{K^{-1}}$

Adapted from:

[1] Kvorka et al. (2018).
[2] Chen et al. (2014).
[3] Gammon et al. (1983).
[4] Hobbs (1974).
[5] Stone and Miner (1989).
[6] Souček et al. (2019).
[7] Kalousová and Sotin (2020).
[8] Nimmo and Spencer (2014).

4.1 Viscosity profiles

First of all, we will recall Eq. (2.27) to compute the viscosity profiles (see Fig. (4.1)) for both conductive and convective heat transfer mechanisms. Nimmo and Spencer (2014) estimate the maximum ice shell thickness on Triton as ≈ 400 km. Despite that, we will conduct our computations even for faintly thicker shells. As we can see, convective models typically have a larger volume in which dissipation can occur; besides, the convective mechanism is generally improbable in thin (i.e., dozens of kilometers) shells.

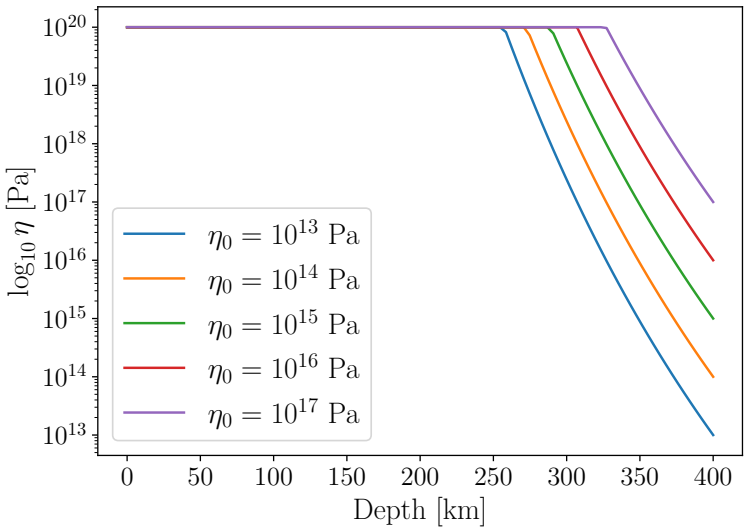

(a) Conductive heat transport.

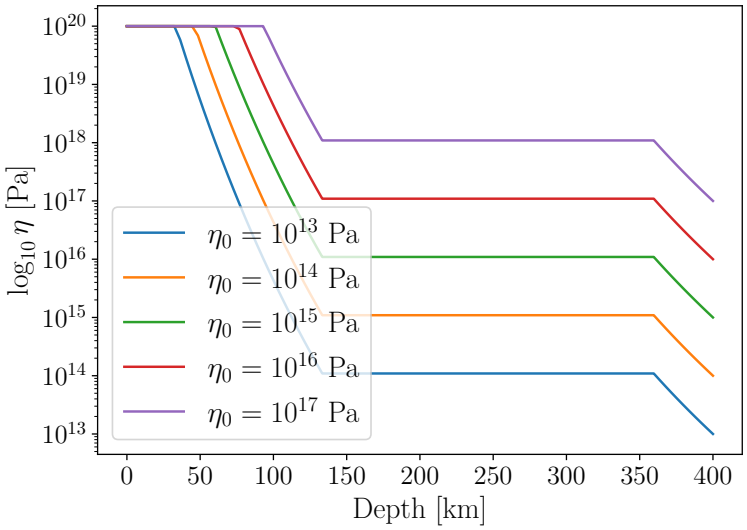

(b) Convective heat transport.

Figure 4.1: Viscosity profiles computed from the temperature profiles of the shell for a selected set of basal viscosities.

4.2 Tidal dissipation

Since the computed tidal heating exhibits the properties of a mechanical damped oscillator, we have to undergo a sufficient number of cycles (Triton's orbital periods) before the tidal power stabilizes. This phenomenon is demonstrated in Fig. 4.2. Indubitably, the convective models are prone to take significantly longer and thus take more of the computation time.

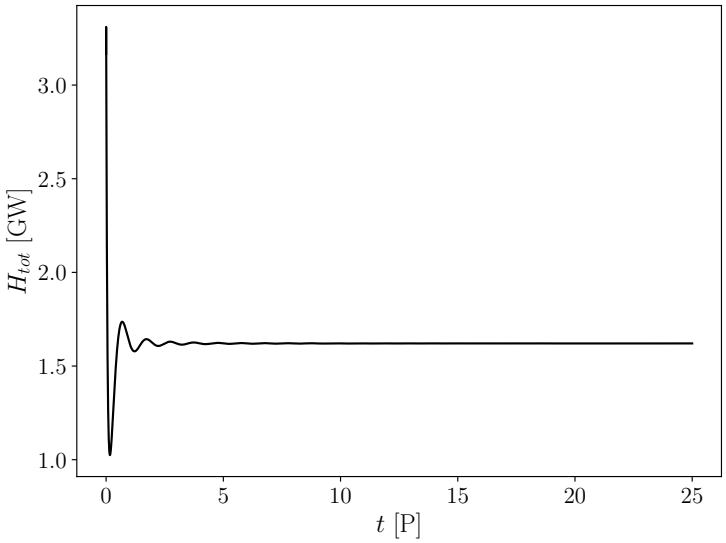

(a) Conductive heat transport.

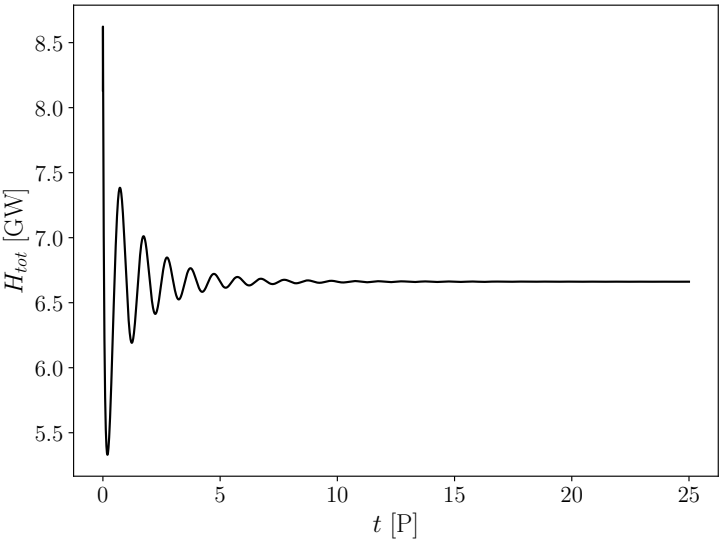

(b) Convective heat transport.

Figure 4.2: The time evolution of the total tidal dissipation before reaching the stable state for a shell of thickness 400 km and basal viscosity $\eta_0 = 10^{14}$ Pa · s.

The parametric study of Triton is represented by two power maps for both heat transport mechanisms for the set of basal viscosities $\eta_0 \in (10^{13} - 10^{17})$ Pa · s and thicknesses $d \in (0 - 500)$ km. Both power maps comprise 10 x 15 models. The conductive models are depicted in Fig. 4.3. Since the studies on Enceladus detected a power spike for shells with a low thickness, we ran a series of calculations (15 x 15) models for the region $d \in (0-50)$ km to investigate whether Triton exhibits the same behavior pattern. We also plotted the Rayleigh number of $\mathrm{Ra} = 10^{10}$, which covers most models with a non-negligible power. With such a high Rayleigh number, we suppose the convective mechanism takes over in this region. Let us assume that the orientation value of the critical Rayleigh number is $\mathrm{Ra}_{cr} \approx 10^5$; that implies that the conductive mechanism occurs mostly for shells with a thickness of $d < 50$ km and high viscosities. In any case, the computed powers for low thickness are marginal at best, and henceforth, we will study the convective models.

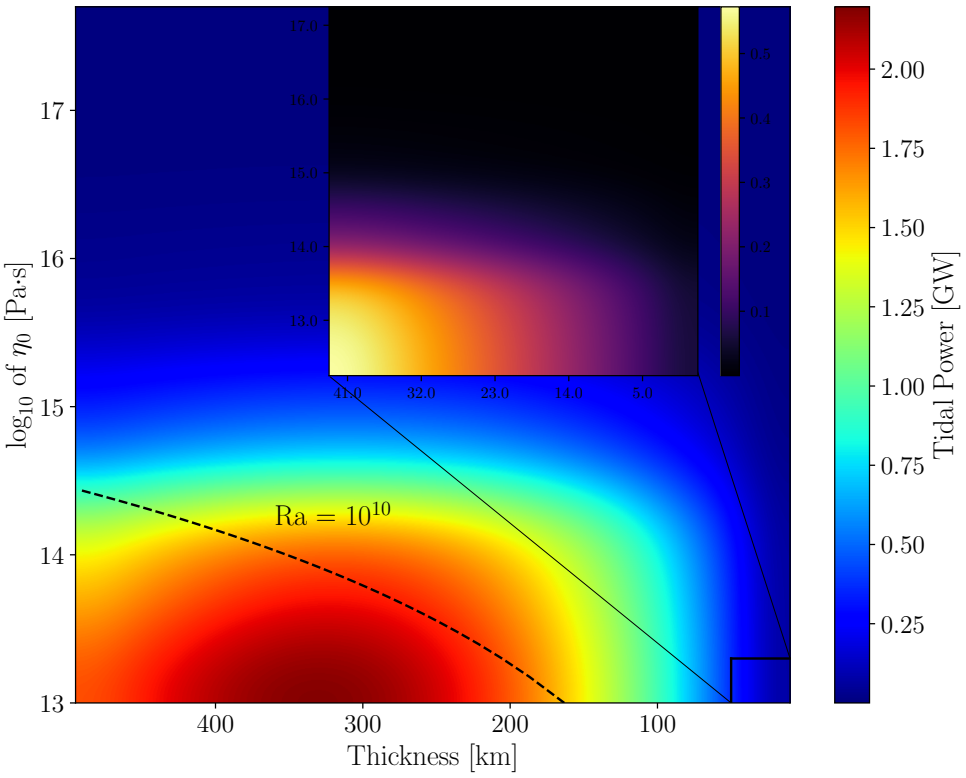

Figure 4.3: Tidal power map (10 x 15 models) for the conductive heat transport (including zoomed region of low thickness).

The power map for the convective models is displayed in Fig. 4.4. We can see a region of models that predicts the tidal dissipation of 5–30 GW for viscosities $\eta_0 \in (10^{13} - 10^{14})$ Pa · s. All models are also compatible with the Rayleigh number and thus can be studied further. In order to associate tidal dissipation with some phenomena observed on the surface (e.g., cryovulcanism or plumes), we selected the most promising model, $\eta_0 = 10^{13}$ Pa · s and $d = 400$ km, and computed

the distribution lateral distribution of the tidal heating according to Eq. (2.31). We used the departmental program computing the double dot product of two tensor spherical harmonics (see Attachment), which yielded only three non-zero coefficients of the spectral expansion, q_{00}, q_{20} and q_{40}. The tidal heat flux can then be reconstructed as

$$q_t(\theta,\phi) = \sum_{j=0}^{\infty}\sum_{m=-j}^{j} q_{jm}Y_{jm}(\theta,\phi) = q_{00}Y_{00} + q_{20}Y_{20} + q_{40}Y_{40}\,, \tag{4.1}$$

we can immediately notice that q_t is independent of longitude. In Fig. 4.5, we can see the tidal flux as a function of colatitude and the tidal dissipation rate (i.e., power per unit volume) as a function of depth. Ultimately, Fig. 4.6 features the tidal heat flux at the surface of Triton mapped to 2D.

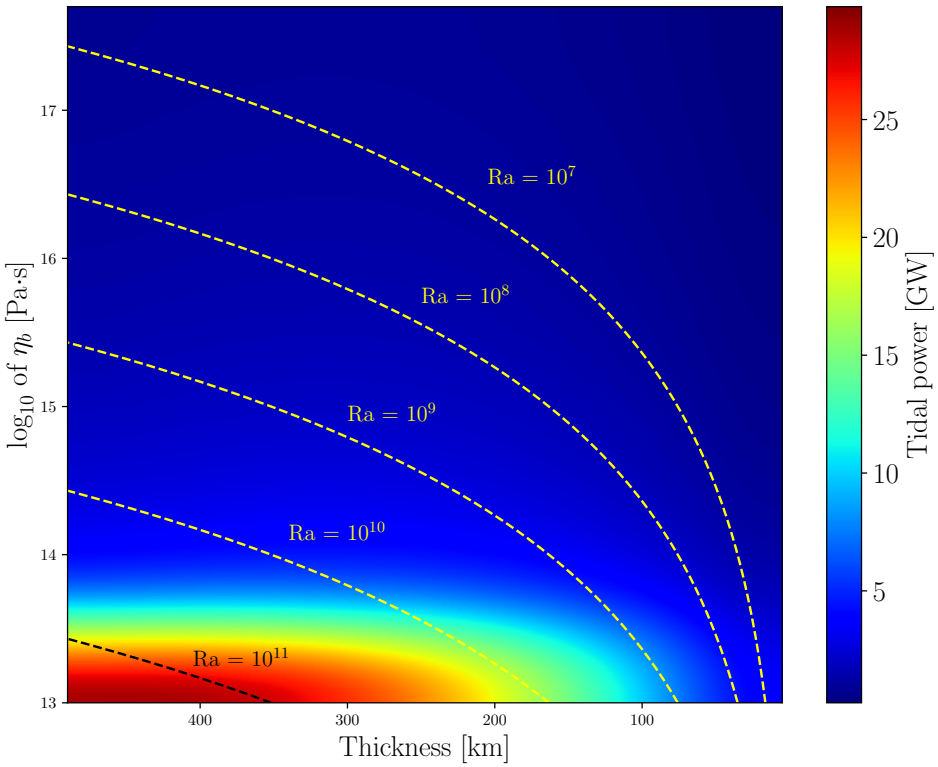

Figure 4.4: Tidal power map (10 x 15 models) for the convective heat transport (including plotted Rayleigh numbers).

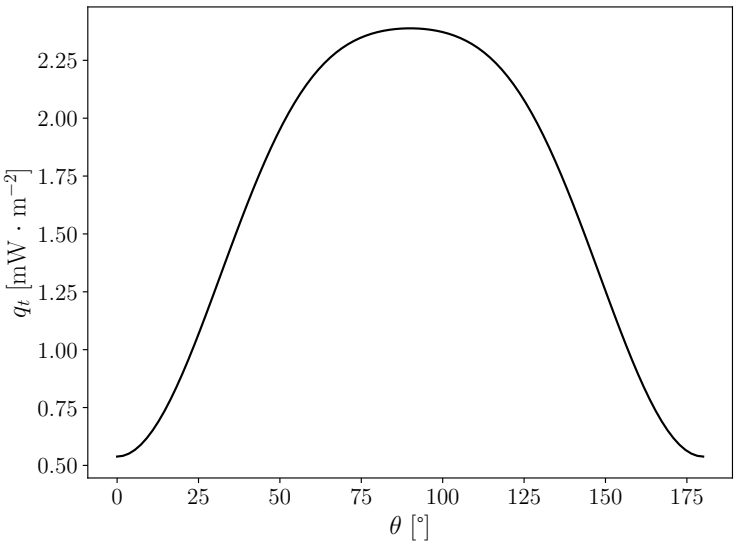

(a) Tidal heat flux.

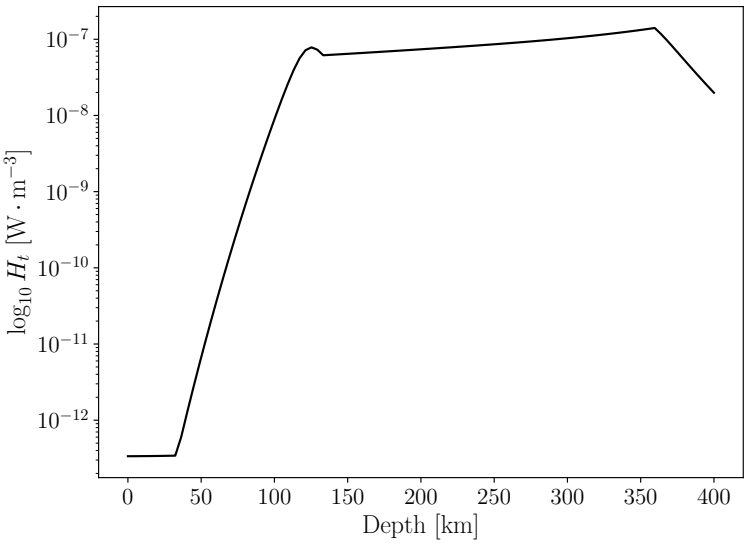

(b) Dissipation rate in the shell for the convective heat transfer.

Figure 4.5: Convective model $\eta_0 = 10^{13}$ Pa · s and $d = 400$ km.

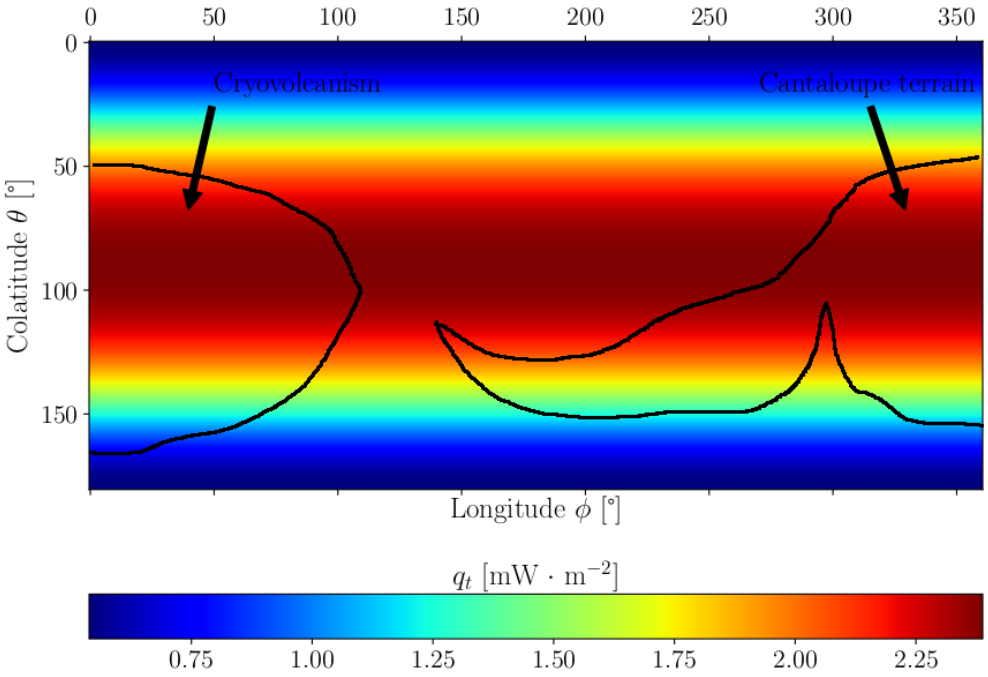

Figure 4.6: Tidal heating rate with Triton's sketched known surface.

4.3 Discussion

We conducted a series of calculations for two heat transfer mechanisms to make a rough estimate of the tidal powers generated within Triton's ice shell. We stress that we had used several assumptions and simplifications; most notably, we assumed time-independent conductivity of ice, and we did not couple the computed tidal heating with the heat equation in the form of a source term. We would need to solve the heat equation separately in each time step, which would have yielded a new temperature profile and thus a new viscosity profile.

Conductive models generally show low tidal powers. There is only a small family of models for which the total tidal dissipation exceeds 2 GW; however, these models are not compatible with huge Rayleigh numbers, and thus the shell is most likely in the convective regime. On the contrary, models corresponding to low Rayleigh numbers predict negligible power (tenths of a gigawatt and less). We also observed that the power attains a maximum at roughly 330 km and then decreases monotonously with depth. Moreover, all computed powers pale in comparison with the expected heat losses of the body due to body radiation, which makes around 29.3 GW for Triton and the presented conductive model.

As for the power map devoted to the convective models, we found a relatively large region of models that predict the power of 5–30 GW and are also compatible. In contrast with the conductive models, where heating is concentrated in the bottom 10−15 % of the shell and is insignificant elsewhere, dissipation is ongoing in most of the shell's volume for convective models. For the selected model ($\eta_0 = 10^{13}$ Pa · s and $d = 400$ km), we also computed the tidal heat flux distribution on

the surface of Triton. We found that most of the tidal heating is concentrated in a relatively wide strip around the equator; there is over 100° of colatitude, where the tidal heat flux is greater than 1.5 $\mathrm{mW \cdot m^{-2}}$. As we approach the poles, the tidal heat flux attenuates to 0.5 $\mathrm{mW \cdot m^{-2}}$. There is a greater temperature gradient at the surface for the convective heat transfer mechanism; the expected heat losses are approximately 87.9 GW, which is somewhat disappointing, for it means that the sole effect of tidal heating in the ice shell can not in all likelihood explain the presence of an ocean (or prevent it from freezing, to be precise). On the other hand, we can see that it can cover 6 % to 35 % of the losses, which is no longer a negligible amount. The lateral distribution of the tidal heat flux also opens the question of whether tidal heating can drive some of the geological activity within Triton. Authors Kirk et al. (1990) believe that the observed geysers on Triton are powered by solar heating, which may be indicated by the fact that most of the plumes are close to the subsolar point. However, there a rich cryovolcanic activity and cantaloupe terrain in the equilateral region, where our models predict the greatest concentration of the heating.

We also should not refrain from commenting on the used constitutive equation. Maxwell rheology model accurately describes the anelastic deformation of the shell on time scales satisfying $\gtrapprox 2\pi\eta/\mu$ (see Efroimsky 2012). Since the orbital period of Triton is about $5 \cdot 10^5$ s, it implies that our results are relevant for viscosities $\approx 10^{14}$ $\mathrm{Pa \cdot s}$ and lower.

Overall, we can state that tidal heating has the potential to provide a reasonable amount of energy (roughly a third of the heat losses in the most convenient scenario) in the energy balance of Triton. This satellite also has a large density compared to other icy moons, which insinuates the presence of an immense silicate core and therefore a potential source of radiogenic heating. We also did not endow the ice shell with any clathrates, which would enhance the insulating properties. As we can see in, e.g., Mitri and Showman (2008), this adjustment can have a massive impact on the thermal conductivity, thus also on the Rayleigh number. Nevertheless, even if tidal heating does not have its share on Triton's subsurface ocean, it does not mean the ocean is not there. For instance, Pluto is often referred to as "Triton's comrade" due to their extreme similarity in both origin and properties and recent study by Bierson et al. (2020) suggests that a body can harbor an ocean even if there is no ongoing tidal dissipation present.

Conclusion

This study was devoted to the process of tidal heating in the Triton's ice shell for obliquity tides. We derived governing equations of the anelastic deformation, utilized the Maxwell rheology model, and employed spectral methods in 3D for a 1D (i.e., radially dependent only) viscosity profile. We developed our program in Python 3 and calculated tidal heating in the shell for a broad spectrum of shell thicknesses and basal viscosities (which corresponds to microscopic properties of the ice, most notably the grain size), represented the models in the form of power contour maps, and discussed their compatibility. Furthermore, we computed the lateral distribution of the heating (i.e., tidal heat flux).

We found that tidal heating on Triton is marginal for the conductive heat transfer, but it can represent up to 30 GW for convective models. Most of the power is concentrated around the equator, which raises the question of whether tidal dissipation can drive the cryovolcanic activity observed in this area. The further studies on Triton may include employing a more complex rheology model (e.g., Andrade rheology model), computing tidal dissipation in the ocean, and solving the convective heat equation.

Appendix A

Spherical harmonics

The following sections A, B, and C are based on the findings presented in Varshalovich et al. (1988); all formulae and the formalism is adapted from this publication.

A.1 Scalar spherical harmonics

The fully-normalized *scalar spherical harmonics* are continuous, complex, and bounded mappings $Y_{jm} : S^2 \to \mathbb{C}$ of degree j and order m characterized by two real variables, colatitude θ and longitude ϕ, and defined by

$$Y_{jm}(\theta,\phi) = \begin{cases} N_{jm} P_{jm}(\cos\theta)\exp(im\phi) & m \geq 0 \\ (-1)^m Y^*_{j,-m}(\theta,\phi) & m < 0 \end{cases} \tag{A.1}$$

where P_{jm} are the associated Legendre polynomials and $j = 0, 1, 2, \ldots, \infty$, $m = -j, \ldots, j$. The normalization factor N_{jm} is defined as

$$N_{jm} = \sqrt{\frac{(2j+1)}{4\pi}\frac{(j-m)!}{(j+m)!}}\,, \tag{A.2}$$

so that the following orthonormality condition holds true

$$\int_\Omega Y_{j_1 m_1} Y^*_{j_2 m_2}\ \mathrm{d}\Omega = \int_0^{2\pi}\int_0^{2\pi} Y_{j_1 m_1} Y^*_{j_2 m_2} \sin\theta\ \mathrm{d}\phi\ \mathrm{d}\theta = \delta_{j_1 j_2}\delta_{m_1 m_2}\,, \tag{A.3}$$

where Ω denotes the surface of a unit sphere and δ is the Kronecker delta.

Every complex and integrable function $f(r,\theta,\phi)$ can be expanded into a harmonic series

$$f(r,\theta,\phi) = \sum_{j=0}^{\infty}\sum_{m=-j}^{j} f_{jm}(r) Y_{jm}(\theta,\phi)\,, \tag{A.4}$$

where f_{jm} are spectral scalar coefficients. Provided that $f(r,\theta,\phi)$ is a real function, the following relation is valid:

$$f_{j,-m} = (-1)^m f^*_{jm}\,, \tag{A.5}$$

and each scalar spherical harmonic has the following property

$$Y_{j-m} = (-1)^m Y_{jm}\,. \tag{A.6}$$

A.2 Vector spherical harmonics

The formalism of spherical harmonics can be extended for vector fields. Let us define a set of Cartesian unit vectors

$$\vec{e}_1 = -\frac{1}{\sqrt{2}}\left(\vec{e}_x + i\vec{e}_y\right) \tag{A.7}$$

$$\vec{e}_{-1} = \frac{1}{\sqrt{2}}\left(\vec{e}_x - i\vec{e}_y\right) \tag{A.8}$$

$$\vec{e}_0 = \vec{e}_z\,, \tag{A.9}$$

with the following properties

$$\vec{e}_\mu^{\,*} = (-1)^\mu \vec{e}_{-\mu}\,, \tag{A.10}$$

$$\vec{e}_\mu^{\,*} \cdot \vec{e}_\nu = \delta_{\mu\nu}\,. \tag{A.11}$$

The *vector spherical harmonics* are then defined by

$$\vec{Y}^{\,l}_{jm} = \sum_{\mu\nu} C^{jm}_{l\nu 1\mu} Y_{l\nu}(\theta,\phi)\vec{e}_\mu\,, \tag{A.12}$$

where $C^{jm}_{l\nu 1\mu}$ are the Clebsch-Gordan coefficients (see Appendix B). For each order j and degree m (with the exception of $j = m = 0$), we have got three corresponding vectors $\vec{Y}^{\,j-1}_{jm}, \vec{Y}^{\,j}_{jm}$, and $\vec{Y}^{\,j+1}_{jm}$. These vectors are not locally orthonormal, however, the global condition of orthonormality is satisfied

$$\int_0^{2\pi}\int_0^{\pi} \vec{Y}^{\,l_1}_{j_1 m_1}(\theta,\phi)\cdot\vec{Y}^{\,l_2}_{j_2 m_2}(\theta,\phi)\sin\theta\;\mathrm{d}\theta\;\mathrm{d}\phi = \delta_{j_1 j_2}\delta_{m_1 m_2}\delta_{l_1 l_2}\,. \tag{A.13}$$

In analogy to scalar functions, we can expand every complex, continuous, and integrable vector field $\vec{f}$ into a series

$$\vec{f}(r,\theta,\phi) = \sum_{j=0}^{\infty}\sum_{m=-j}^{j}\sum_{l=|j-1|}^{j+1} f^l_{jm}(r)\vec{Y}^{\,l}_{jm}(\theta,\phi)\,, \tag{A.14}$$

where f^l_{jm} are the vector spectral coefficients defined by

$$f^l_{jm}(r) = \int_0^{2\pi}\int_0^{\pi} \vec{f}(r,\theta,\phi)\cdot\vec{Y}^{\,l*}_{jm}(\theta,\phi)\sin\theta\;\mathrm{d}\theta\;\mathrm{d}\phi\,. \tag{A.15}$$

Moreover, the vector spectral coefficients for real vector fields $\vec{f}$ satisfy

$$f^l_{j,-m} = (-1)^{j+m+l+1} f^{l*}_{jm}\,, \tag{A.16}$$

and each vector spherical harmonic has the following property

$$\vec{Y}^{\,l}_{j-m} = (-1)^{j+m+l+1}\vec{Y}^{\,l*}_{jm}\,. \tag{A.17}$$

A.3 Tensor spherical harmonics

Ultimately, let us define the following tensor base

$$\mathbf{e}_{k\lambda} = \sum_{\mu\nu} C^{k\lambda}_{1\mu 1\nu} \vec{e}_\mu \vec{e}_\nu \,, \tag{A.18}$$

where $k = 0, 1, 2$ and $\lambda = -k, \ldots, k$. The *tensor spherical harmonics* are then naturally given by

$$\mathbf{Y}^{lk}_{jm}(\theta, \phi) = \sum_{\mu\nu} C^{jm}_{l\mu k\nu} Y_{l\mu}(\theta, \phi) \mathbf{e}_{k\nu} \,, \tag{A.19}$$

where $k = 0, 1, 2$ and $l = |j-k|, \ldots, j+k$. The global condition of orthonormality for tensor harmonics reads

$$\int_0^{2\pi} \int_0^{\pi} \mathbf{Y}^{l_1 k_1}_{j_1 m_1}(\theta, \phi) : \mathbf{Y}^{l_2 k_2}_{j_2 m_2}(\theta, \phi) \sin\theta \, \mathrm{d}\theta \, \mathrm{d}\phi = \delta_{j_1 j_2} \delta_{m_1 m_2} \delta_{l_1 l_2} \delta_{k_1 k_2} \,. \tag{A.20}$$

Every complex, continuous, and integrable tensor function $\boldsymbol{F}$ can be expanded into a series

$$\boldsymbol{F}(r, \theta, \phi) = \sum_{j=0}^{\infty} \sum_{m=-j}^{j} \sum_{k=0}^{2} \sum_{l=|j-k|}^{j+k} F^{lk}_{jm}(r) \mathbf{Y}^{lk}_{jm}(\theta, \phi) \,, \tag{A.21}$$

where F^{kl}_{jm} are tensor spectral coefficients given by

$$F^{lk}_{jm}(r) = \int_0^{2\pi} \int_0^{\pi} \mathbf{F}(r, \theta, \phi) : \boldsymbol{Y}^{lk*}_{jk}(\theta, \phi) \sin\theta \, \mathrm{d}\theta \, \mathrm{d}\phi \,, \tag{A.22}$$

and for real tensor fields

$$F^{lk}_{j-m} = (-1)^{j+m+l+k} F^{lk*}_{jm} \,, \tag{A.23}$$

holds. Each tensor spherical harmonic has the following property

$$\boldsymbol{Y}^{kl}_{j-m} = (-1)^{j+m+l+k} \boldsymbol{Y}^{lk*}_{jm} \,. \tag{A.24}$$

Appendix B

Clebsch-Gordan coefficients and Wigner symbols

B.1 Clebsch-Gordan coefficients

In the previous section, we found ourselves in need of a new mathematical object; Clebsch-Gordan coefficients $C^{jm}_{j_1m_1j_2m_2}$ are ubiquitous in the calculus of spherical harmonics and have the following properties:

- They are non-zero if and only if
  1. $j \geq 0$, $j_1 \geq 0$, $j_2 \geq 0$,
  2. $|m| \leq j$, $|m_1| \leq j_1$, $|m_2| \leq j_2$,
  3. triangle inequality: $|j_1 - j_2| \leq j \leq j_1 + j_2$,
  4. $m = m_1 + m_2$,
  5. if $m = m_1 = m_2 = 0$, then $j + j_1 + j_2$ must be even ,

  are satisfied simultaneously.

- Symmetry:
  1. $C^{jm}_{j_1m_1j_2m_2} = (-1)^{j+j_1+j_2} C^{j-m}_{j_1-m_1j_2-m_2} = (-1)^{j+j_1+j_2} C^{jm}_{j_2m_2j_1m_1}$,
  2. $C^{jm}_{j_1m_1j_2m_2} = (-1)^{j_1+m_1} \frac{\Pi_j}{\Pi_{j_2}} C^{j_2,-m_2}_{j_1m_1jm} = (-1)^{j_1+m_2} \frac{\Pi_j}{\Pi_{j_2}} C^{j_2m_2}_{jmj_1-m_1}$,
  3. $C^{jm}_{j_1m_1j_2m_2} = (-1)^{j_2+m_2} \frac{\Pi_j}{\Pi_{j_1}} C^{j_1-m_1}_{j-mj_2m_2} = (-1)^{j_2+m_2} \frac{\Pi_j}{\Pi_{j_1}} C^{j_1m_1}_{j2-m_2jm}$,

  where $\Pi_{j_1,j_2,\ldots,j_n} = \Pi_{j=j_1}^{j_n} \sqrt{2j+1}$.

- Special values and the general formula:
  1. $C^{jm}_{j_1m_1,00} = \delta_{j_1j}\delta_{m_1m}$, $C^{00}_{j_1m_1j_2m_2} = \frac{(-1)^{j_1+m_1}}{\Pi_{j_1}} \delta_{j_1,j_2}\delta_{m_1,-m_2}$,
  2.

$$C^{c\gamma}_{a\alpha b\beta} = \delta_{\gamma,\alpha+\beta} \left[\frac{(a+b-c)!\,(a-b+c)!\,(-a+b+c)!}{(a+b+c+1)!} \right] \qquad \text{(B.1)}$$
$$\times \left[(a+\alpha)!\,(a-\alpha)!\,(b+\beta)!\,(b-\beta)!\,(c+\gamma)!\,(c-\gamma)!\,(2c+1) \right]^{1/2}$$
$$\times \sum_z \frac{(-1)^z}{z!\,(a+b-c-z)!\,(a-\alpha-z)!\,(b+\beta-z)!\,(c-b+\alpha+z)!\,(c-\alpha-\beta+z)!}$$

B.2 Wigner symbols

The Wigner 3-j symbols are defined as follows:

$$\begin{pmatrix} j_1 & j_2 & j \\ m_1 & m_2 & -m \end{pmatrix} = \frac{(-1)^{j+m}}{\Pi_j} C^{jm}_{j_1,-m_1 j_2,-m_2} \tag{B.2}$$

The 3-j symbols are an alternative to Clebsch-Gordan coefficients, and the very same rules for non-zeroness hold here as well.

The Wigner 6-j symbols are usually defined by the following relation

$$(-1)^{j_1+l_2+l_3}\Pi_{j_3 l_3} C^{j_1 m_1}_{j_2 m_2 j_3 m_3} \begin{Bmatrix} l_1 & l_2 & j_3 \\ j_1 & j_2 & l_3 \end{Bmatrix} = \sum_{n_1 n_2 n} C^{j_3 m_3}_{l_1 n_1 l_2 n_2} C^{j_1 m_1}_{l_3 n_3 l_2 n_2} C^{l_3 n_3}_{l_1 n_1 j_2 m_2}\,, \tag{B.3}$$

and they are invariant to an arbitrary permutation of columns and rows. The Wigner 6-j symbols often occur in the calculus of spherical harmonics, and therefore, we will list several values (which we will use in the next section) of the symbols for special choices of the Clebsch-Gordan coefficients:

$$\begin{Bmatrix} j_1 & j_2 & j \\ l_1 & l_2 & 0 \end{Bmatrix} = \frac{(-1)^{j_1+j_2+j}}{\Pi_{j_1 j_2}} \delta_{j_1 l_2} \delta_{j_2 l_1}\,, \tag{B.4}$$

$$\begin{Bmatrix} j & 2 & j-2 \\ 1 & j-1 & 1 \end{Bmatrix} = \frac{1}{\sqrt{5(2j-1)}}\,, \tag{B.5}$$

$$\begin{Bmatrix} j_1 & j_2 & j \\ l_1 & l_2 & 0 \end{Bmatrix} = \frac{1}{\sqrt{5(2j-1)}}\,, \tag{B.6}$$

$$\begin{Bmatrix} j & j & 2 \\ 1 & 1 & j-1 \end{Bmatrix} = \sqrt{\frac{(j+1)(2j+3)}{30j(2j-1)(2j+1}}\,, \tag{B.7}$$

$$\begin{Bmatrix} j & j & 2 \\ 1 & 1 & j+1 \end{Bmatrix} = \sqrt{\frac{j(2j-1)}{(2j+3)(j+1)(2j+1)}}\,, \tag{B.8}$$

$$\begin{Bmatrix} j & 1 & j \\ 2 & j+1 & 1 \end{Bmatrix} = -\sqrt{\frac{j+2}{10(j+1)(2j+1)}}\,, \tag{B.9}$$

$$\begin{Bmatrix} j & 1 & j \\ 2 & j-1 & 1 \end{Bmatrix} = -\sqrt{\frac{j-1}{10j(2j+1)}}\,, \tag{B.10}$$

$$\begin{Bmatrix} j & j & 1 \\ 1 & 1 & j+1 \end{Bmatrix} = \sqrt{\frac{j}{6(j+1)(2j+1)}}\,, \tag{B.11}$$

$$\begin{Bmatrix} j & j & 2 \\ 1 & 1 & j-1 \end{Bmatrix} = \sqrt{\frac{j+1}{6j(2j+1)}}\,. \tag{B.12}$$

Appendix C

Identities

Material derivative operator:

$$\frac{D\bullet}{Dt} = \begin{cases} \frac{\partial \bullet}{\partial t} & \text{Lagrangian description} \\ \frac{\partial \bullet}{\partial t} + \vec{v} \cdot \nabla \bullet & \text{Eulerian description} \end{cases} \tag{C.1}$$

C.1 Calculus of spherical harmonics

Differential operators:

$$\nabla \left[f(r) Y_{jm} \right] = \frac{1}{\sqrt{2j+1}} \left[\sqrt{j} \left(\frac{\mathrm{d}}{\mathrm{d}r} + \frac{j+1}{r} \right) f(r) \vec{Y}^{j-1}_{jm} - \sqrt{j+1} \left(\frac{\mathrm{d}}{\mathrm{d}r} - \frac{j}{r} \right) f(r) \vec{Y}^{j+1}_{jm} \right], \tag{C.2}$$

$$\nabla \cdot \left[f(r) \vec{Y}^{l}_{jm} \right] = \frac{1}{\sqrt{2j+1}} \left[\sqrt{j} \left(\frac{\mathrm{d}}{\mathrm{d}r} - \frac{j-1}{r} \right) \delta_{l,j-1} - \sqrt{j+1} \left(\frac{\mathrm{d}}{\mathrm{d}r} + \frac{j+2}{r} \right) \delta_{l,j+1} \right] f(r) Y_{jm}, \tag{C.3}$$

$$\begin{aligned} \nabla \left[f(r) \vec{Y}^{l}_{jm} \right] = (-1)^{j+l+1} \sum_k \sqrt{2k+1} \sqrt{l} \begin{Bmatrix} 1 & 1 & k \\ j & l-1 & l \end{Bmatrix} \times \\ \times \left(\frac{\mathrm{d}}{\mathrm{d}r} + \frac{l+1}{r} \right) f(r) \mathbf{Y}^{l-1,k}_{jm} + (-1)^{j+l} \sum_k \sqrt{2k+1} \sqrt{l+1} \times \\ \begin{Bmatrix} 1 & 1 & k \\ j & l+1 & l \end{Bmatrix} \left(\frac{\mathrm{d}}{\mathrm{d}r} - \frac{l}{r} \right) f(r) \mathbf{Y}^{l+1,k}_{jm}, \end{aligned} \tag{C.4}$$

$$\nabla \cdot \left[f(r) \mathbf{Y}^{lk}_{jm} \right] = (-1)^{j+l} \sqrt{2k+1} \times \left[\sqrt{l+1} \begin{Bmatrix} 1 & l & l+1 \\ j & 1 & k \end{Bmatrix} \left(\frac{\mathrm{d}}{\mathrm{d}r} - \frac{l}{r} \right) f(r) \vec{Y}^{l+1}_{jm} - \sqrt{l} \begin{Bmatrix} 1 & l & l-1 \\ j & 1 & k \end{Bmatrix} \left(\frac{\mathrm{d}}{\mathrm{d}r} + \frac{l+1}{r} \right) f(r) \vec{Y}^{l-1}_{jm} \right], \tag{C.5}$$

$$\nabla \cdot \left[f(r) \mathbf{Y}^{j0}_{jm} \right] = \sqrt{\frac{j+1}{3(2j+1)}} \left(\frac{\mathrm{d}}{\mathrm{d}r} - \frac{j}{r} \right) f(r) \vec{Y}^{j+1}_{jm} - \sqrt{\frac{j}{3(2j+1)}} \left(\frac{\mathrm{d}}{\mathrm{d}r} + \frac{j+1}{r} \right) f(r) \vec{Y}^{j-1}_{jm} , \tag{C.6}$$

$$\nabla \cdot \left[f(r) \mathbf{Y}^{j-2,2}_{jm} \right] = \sqrt{\frac{j-1}{2j-1}} \left(\frac{\mathrm{d}}{\mathrm{d}r} - \frac{j-2}{r} \right) f(r) \vec{Y}^{j-1}_{jm} , \tag{C.7}$$

$$\nabla \cdot \left[f(r) \mathbf{Y}^{j-1,2}_{jm} \right] = \sqrt{\frac{j-1}{2(2j+1)}} \left(\frac{\mathrm{d}}{\mathrm{d}r} - \frac{j-1}{r} \right) f(r) \vec{Y}^{j}_{jm} , \tag{C.8}$$

$$\nabla \cdot \left[f(r) \mathbf{Y}^{j2}_{jm} \right] = -\sqrt{\frac{(j+1)(2j+3)}{6(2j-1)(2j+1)}} \left(\frac{\mathrm{d}}{\mathrm{d}r} + \frac{j+1}{r} \right) f(r) \vec{Y}^{j-1}_{jm} + \sqrt{\frac{j(2j-1)}{6(2j+1)(2j+3)}} \left(\frac{\mathrm{d}}{\mathrm{d}r} - \frac{j}{r} \right) f(r) \vec{Y}^{j+1}_{jm} , \tag{C.9}$$

$$\nabla \cdot \left[f(r) \mathbf{Y}^{j+1,2}_{jm} \right] = -\sqrt{\frac{j+2}{2(2j+1)}} \left(\frac{\mathrm{d}}{\mathrm{d}r} + \frac{j+2}{r} \right) f(r) \vec{Y}^{j}_{jm} , \tag{C.10}$$

$$\nabla \cdot \left[f(r) \mathbf{Y}^{j+2,2}_{jm} \right] = -\sqrt{\frac{j+2}{2j+3}} \left(\frac{\mathrm{d}}{\mathrm{d}r} + \frac{j+3}{r} \right) f(r) \vec{Y}^{j+1}_{jm} . \tag{C.11}$$

Products of spherical harmonics and a radial unit vector:

$$\vec{e}_r Y_{jm} = \frac{1}{\sqrt{2j+1}} \left(\sqrt{j}\ \delta_{l,j-1} - \sqrt{j+1}\ \delta_{l,j+1} \right) \vec{Y}^{l}_{jm} , \tag{C.12}$$

$$\vec{e}_r \cdot \vec{Y}^{l}_{jm} = \frac{1}{\sqrt{2j+1}} \left(\sqrt{j}\ \delta_{l,j-1} - \sqrt{j+1}\ \delta_{l,j+1} \right) Y_{jm} , \tag{C.13}$$

$$\vec{e}_r \cdot \mathbf{Y}^{ln}_{jm} = (-1)^{j+l}\ \sqrt{2n+1}\ \left[\sqrt{l+1} \begin{Bmatrix} l & n & j \\ 1 & l+1 & 1 \end{Bmatrix} \vec{Y}^{l+1}_{jm} - \sqrt{l} \begin{Bmatrix} l & n & j \\ 1 & l-1 & 1 \end{Bmatrix} \vec{Y}^{l-1}_{jm} \right] , \tag{C.14}$$

$$\vec{e}_r \cdot \mathbf{Y}^{j0}_{jm} = \frac{1}{\sqrt{3(2j+1)}} \left(\sqrt{j+1}\ \vec{Y}^{j+1}_{jm} - \sqrt{j}\ \vec{Y}^{j-1}_{jm} \right) , \tag{C.15}$$

$$\vec{e}_r \cdot \mathbf{Y}^{j-2,2}_{jm} = \sqrt{\frac{j-1}{2j-1}}\ \vec{Y}^{j-1}_{jm} , \tag{C.16}$$

$$\vec{e}_r \cdot \mathbf{Y}^{j-1,2}_{jm} = \sqrt{\frac{j-1}{2(2j+1)}}\ \vec{Y}^{j}_{jm} , \tag{C.17}$$

$$\vec{e}_r \cdot \mathbf{Y}_{jm}^{j,2} = \sqrt{\frac{j(2j-1)}{2.3.(2j+1)(2j+3)}}\ \vec{Y}_{jm}^{j+1} - \sqrt{\frac{(j+1)(2j+3)}{2.3.(2j+1)(2j-1)}}\vec{Y}_{jm}^{j-1}\,, \quad \text{(C.18)}$$

$$\vec{e}_r \cdot \mathbf{Y}_{jm}^{j+1,2} = -\sqrt{\frac{j+2}{2(2j+1)}}\ \vec{Y}_{jm}^{j}\,, \quad \text{(C.19)}$$

$$\vec{e}_r \cdot \mathbf{Y}_{jm}^{j+2,2} = -\sqrt{\frac{j+2}{2j+3}}\ \vec{Y}_{jm}^{j+1}\,. \quad \text{(C.20)}$$

Appendix D

Radial discretization

Table D.1: Coefficients of the discretized equations

$a_1 = \sqrt{\frac{j}{2j+1}}$	$a_2 = -(j-1)a_1$	$b_1 = -\sqrt{\frac{j+1}{2j+1}}$
$b_2 = (j+2)b_1$	$c_1 = -\sqrt{\frac{j}{3(2j+1)}}$	$c_2 = (j+1)c_1$
$d_1 = \sqrt{\frac{j-1}{2j-1}}$	$d_2 = -(j-2)d_1$	$e_1 = -\sqrt{\frac{(j+1)(2j+3)}{6(2j-1)(2j+1)}}$
$e_2 = -(j+1)e_1$	$g_1 = \sqrt{\frac{j(2j-1)}{6(2j+1)(2j+3)}}$	$g_2 = -jg_1$
$h_1 = -\sqrt{\frac{j+2}{2j+3}}$	$h_2 = (j+3)h_1$	$f_1 = \sqrt{\frac{j+1}{3(2j+1)}}$
$f_2 = -jf_2$	$p_1 = \sqrt{\frac{j-1}{2j-1}}$	$p_2 = jp_1$
$s_1 = -\sqrt{\frac{j+2}{2j+3}}$	$s_2 = -(j+1)s_1$	$r_1 = \sqrt{\frac{j(2j-1)}{6(2j+1)(2j+3)}}$
$r_2 = (j+2)r_1$	$q_1 = -\sqrt{\frac{(j+1)(2j+3)}{6(2j-1)(2j+1)}}$	$q_2 = -(j-1)q_1$
$z_1 = \rho_i g_s \frac{j}{2j+1}$	$z_2 = -\rho_i g_s \sqrt{\frac{j(j+1)}{2j+1}}$	$z_3 = -\sqrt{\frac{j}{3(2j+1)}}$
$z_4 = \sqrt{\frac{j-1}{2j-1}}$	$z_5 = -\sqrt{\frac{(j+1)(2j+3)}{6(2j+1)(2j-1)}}$	$w_1 = -\rho_i g_s \sqrt{\frac{j(j+1)}{2j+1}}$
$w_2 = \rho_i g_s \frac{j+1}{2j+1}$	$w_3 = \sqrt{\frac{j+1}{3(2j+1)}}$	$x_1 = \Delta\rho g_b \frac{j}{2j+1}$
$x_2 = -\Delta\rho g_b \sqrt{\frac{j(j+1)}{2j+1}}$	$x_3 = \sqrt{\frac{j}{3(2j+1)}}$	$x_4 = -\sqrt{\frac{j-1}{2j-1}}$
$x_5 = \sqrt{\frac{(j+1)(2j+3)}{6(2j+1)(2j-1)}}$	$y_1 = -\Delta\rho g_b \sqrt{\frac{j(j+1)}{2j+1}}$	$y_2 = \Delta\rho g_b \sqrt{\frac{j+1}{2j+1}}$
$y_3 = -\sqrt{\frac{j+1}{3(2j+1)}}$	$y_4 = -\sqrt{\frac{j(2j-1)}{6(2j+1)(2j+3)}}$	$y_5 = \sqrt{\frac{j+2}{2j+3}}$
$\delta_1 = \sqrt{\frac{j}{2j+1}}$	$\delta_2 = -\sqrt{\frac{j+1}{2j+1}}$	

Note: $\Delta\rho = \rho_w - \rho_i$.

Attachment

Tidal dissipation

The attached program is written in Python 3. The key part of the program are separate solvers for elastic and viscoelastic (Maxwell) rheology. The user calls functions `elastic_solver()` and `viscoelastic_solver()` with the following arguments:

- `viscoelastic_solver`: Radii R_{bot} and R_{top}, basal viscosity η_0, heat transfer model (0 for convective, 1 for conductive), the surface and bottom temperatures T_{top} and T_{bot}, number of layers N and the gravitational acceleration at the bottom boundary g_b.
- `elsatic_solver`: Radii R_{bot} and R_{top}.

Double dot product of tensor harmonics

The departmental Fortran program computes the following:

$$\begin{aligned}\mathbf{Y}^{l_1 n_1}_{j_1 m_1} : \mathbf{Y}^{l_2 n_2}_{j_2 m_2} \\ &= \delta_{n_1 n_2}(-1)^{j_2+l_2}\frac{\Pi_{j_1 j_2 l_1 l_2}}{\sqrt{4\pi}}\sum_{jm}\frac{1}{\Pi_j}\,C^{j0}_{l_1 0\ l_2 0}\,C^{jm}_{j_1 m_1\ j_2 m_2} \\ &\quad \begin{Bmatrix} n_1 & l_1 & j_1 \\ j & j_2 & l_2 \end{Bmatrix} Y_{jm}\,.\end{aligned} \tag{D.1}$$

Bibliography

C. J. Bierson, F. Nimmo, and S. A. Stern. Evidence for a hot start and early ocean formation on Pluto. *Nature Geoscience*, 13:468–472, 2020.

E. M. A. Chen, F. Nimmo, and G. A. Glatzmaier. Tidal heating in icy satellite oceans. *Icarus*, 229:11–30, 2014.

D. Cruikshank. *Neptune and Triton*. University of Arizona Press, Tucson, AZ, 2016.

M. Efroimsky. Tidal dissipation compared to seismic dissipation: in small bodies, earths, and super-earths. *Astrophysical Journal*, 746:150, 2012.

P. H. Gammon, H. Kiefte, M. J. Clouter, and W. W. Denner. Elastic constants of artificial and natural ice samples by Brillouin spectroscopy. *Journal of Glaciology*, 29:433–460, 1983.

D. Goldsby and D. Kohlstedt. Superplastic deformation of ice: Experimental observations. *Journal of Geophysical Research: Solid Earth*, 106, 2001.

P. V. Hobbs. *Ice Physics*. Oxford Univ. Press, 1974.

K. Kalousová and C. Sotin. The insulating effect of methane clathrate crust on Titan's thermal evolution. 47:e2020GL087481, 2020.

R. L. Kirk, R. H. Brown, and L. A. Soderblom. Subsurface energy storage and transport for solar-powered geysers on Triton. *Science*, 250(4979):424–429, 1990.

J. Kvorka, O. Čadek, G. Tobie, and G. Choblet. Does Titan's long-wavelength topography contain information about subsurface ocean dynamics? *Icarus*, 310:149–164, 2018.

J. Lipps, G. Delory, Joe Pitmand, and S. Rieboldta. Astrobiology of Jupiter's icy moons. *Proceedings of SPIE - The International Society for Optical Engineering*, 5555, 2004.

Z. Martinec. *Principles of Continuum Mechanics*. Nečas Center Series. Springer Nature, Cham, Switzerland, 1 edition, 2019.

R. L. McKinnon, W. B.; Kirk. *Encyclopedia of the Solar System*. Elsevier Science Publishing, Philadelphia, PA, 3 edition, 2014.

G. Mitri and A. Showman. Thermal convection in ice-i shells of Titan and Enceladus. *Icaru*, 193:387–396, 2008.

F. Nimmo and J. Spencer. Powering Triton's recent geological activity by obliquity tides: Implications for Pluto geology. *Icarus*, 246, 2014.

Photojournal.jpl.nasa.gov. Photojournal: NASA's Image Access Home Page, 2015. URL `https://photojournal.jpl.nasa.gov/`. [Online; accessed 08-May-2022].

P. M. Schenk and K. Zahnle. On the negligible surface age of Triton. *Icarus*, 192: 135–149, 2007.

O. Souček, M. Běhounková, O. Čadek, J. Hron, G. Tobie, and G. Choblet. Tidal dissipation in Enceladus' uneven, fractured ice shell. *Icarus*, 328:218–231, 2019.

E. C. Stone and E. D. Miner. The voyager 2 encounter with the Neptunian system. *Science*, 246:1417–1421, 1989.

G. Tobie, O. Čadek, and C. Sotin. Solid tidal friction above a liquid water reservoir as the origin of the south pole hotspot on Enceladus. *Icarus*, 196: 642–652, 2008.

R. Tyler. Tidal dynamical considerations constrain the state of an ocean on Enceladus. *Icarus*, 211:770–779, 2011.

D. A. Varshalovich, A. N. Moskalev, and V. K. Khersonskii. Quantum theory of Angular Momentum. World Scientific, 1988.

D. Vokrouhlický, D. Nesvorný, and H. F. Levison. Irregular satellite capture by exchange reactions. *Astronomical Journal*, 136:1463–1476, 2008.

Wikipedia. Triton (moon) — Wikipedia, the free encyclopedia, 2022. URL `http://en.wikipedia.org/w/index.php?title=Triton%20(moon)&oldid=1083779462`. [Online; accessed 08-May-2022].

O. Čadek, K. Kalousová, J. Kvorka, and C. Sotin. The density structure of Titan's outer ice shell. *Icarus*, 364:114466, 2021.

List of Figures

List of Tables